

Analysis of Unsteady Behavior in Shock/Turbulent Boundary Layer Interactions with Large-Eddy Simulations

Nathan J. Mullenix* and Datta V. Gaitonde†

Department of Mechanical and Aerospace Engineering, The Ohio State University, Columbus, OH 43210

Various numerical and physical aspects of shock/turbulent boundary layer interactions (STBLI) are discussed in the context of Large-Eddy Simulations (LES). A spatially developing incoming equilibrium turbulent boundary layer is obtained with a force based tripping mechanism. Previous results are augmented with a detailed analysis of this procedure. In particular, it is shown that relatively coarser meshes may be employed if the strength of the trip is increased, together with an adjustment of the wall thermal condition for a short distance downstream of the trip. This approach yields both adiabatic as well as constant wall temperature results. Additionally, it is shown that precursor events provide estimates for the size of the trip with only a small portion of the domain in the vicinity of the trip, thus yielding an efficient technique. A simulation of a STBLI using this spatially developing incoming turbulent boundary layer confirms the low frequency signal observed in the STBLI by other approaches which use recycling techniques, and reproduces the particular unsteadiness shown in a reference experiment. A detailed analysis is performed of the evolution of the Reynolds stresses through the interaction. The amplification of turbulence energy is quantified, and the evolution of two point correlations is explored. The results indicate that the spanwise decorrelation distance first decreases and then increases through the interaction. A preliminary assessment of the effect of pulsed arc filament based actuators is provided. The results indicate a reduction in the separation length when pulsed at a St corresponding to the peak frequency near the reattachment point.

Nomenclature

$C_{\alpha\alpha}$	averaged two point correlations in a given direction
D_c	ratio between electrical and inertial forces
$E_{\alpha\alpha}$	one-dimensional power spectrum
e_c	electronic charge
\mathbf{F}_I	inviscid flux vector
\mathbf{F}_V	viscous flux vector
H	shape factor
$R_{\alpha_r\alpha_s}$	two point correlation between points r and s
\mathbf{S}	source vector
\mathbf{U}	solution vector

Symbols

α	collision efficiency factor; arbitrary flow variable
$\delta_{99,0}$	measured incoming boundary layer thickness
δ_{99}	boundary layer thickness for $u = 0.99U_\infty$
δ^*	displacement thickness
ε	effective duty cycle of DBD actuator
ρ_c	charge density
θ	frequency of the applied voltage for DBD; momentum thickness

*Postdoctoral Researcher, AIAA Member

†Professor, AIAA Fellow

I. Introduction

Shock/turbulent boundary layer interactions occur in nearly all supersonic flows, typically with adverse consequences. In aircraft inlets for example, the compression process occurs through shock waves, which interact with boundary layers on adjacent surfaces (swept) or on opposite surfaces (impinging). Similarly a ramp placed in a supersonic flow also yields a STBLI. The results of STBLI include separation, formation of vortical structures and significant unsteadiness which may yield loss of control authority, propulsion efficiency and structural damage.

Extensive discussions of STBLI may be found in the literature. Overviews may be found in Refs. 1, 2. In recent years, the focus has shifted to the unsteadiness observed in such interactions. Recent experimental data has been presented in, for example, Refs. 2–5. These have collectively shown that for nominally 2-D flows such as when a planar shock impinges on a turbulent boundary layer, or the turbulent boundary layer encounters a 2-D ramp, and separation is induced, lower frequency phenomena are excited. That is, spectra of say the pressure on the surface show the clear existence of a range of excited frequencies which are much lower than those associated with the turbulence in the incoming boundary layer. Two primary mechanisms have been proposed from experimental observations. In Ref. 6 the low frequency signal is correlated with upstream long superstructures in the turbulent boundary layer. Dussauge *et al.*³ performed detailed experimental analyses to propose a mechanism based on separated shear layer instability which causes a fluctuation in the size of the separation bubble.

Several computations have reproduced the low frequency unsteadiness, including Refs. 7–15. Unsteadiness of this type cannot be reproduced with Reynolds Averaged Navier-Stokes (RANS) approaches. Therefore, the methods of choice have been LES or DNS. Detailed analyses of STBLI with higher-fidelity methods have been presented by Pirozzoli *et al.*,¹⁰ Martin *et al.*^{9,13} and Touber and Sandham.^{11,12} These have collectively reproduced the low frequency unsteadiness and have provided a detailed analysis of the spectra in the interaction region.

In this paper, we address the two main aspects of such simulations: 1) generating a clean upstream turbulent boundary layer that satisfies all expected properties and 2) simulating an STBLI with this profile with a view to exploring some of its key properties in terms of Reynolds stress evolution and coherent structures through the interaction. A preliminary assessment of a plasma-actuator controlled STBLI is also presented.

A highly challenging aspect of simulating STBLI with LES or DNS is the need to specify the undisturbed boundary layer. Two significant issues arise. First, it is difficult to simulate the actual transition process in the wind tunnel, both from the standpoint of computational expense as well as a lack of knowledge of the particular disturbance environment related to transition. For this reason, simulations typically provide an artificially generated turbulent boundary layer. A second, equally difficult aspect, stems from the fact that computational expense increases as a relatively high power of Reynolds number (about 4). From a resource constraint standpoint therefore, typical analyses are conducted at Reynolds numbers that are substantially smaller than those in the experiment – typically, the ratio is about one tenth. As such, the signature of the mechanism by which the incoming equilibrium boundary layer is initiated or developed has the potential to contaminate the flow field.

A third constraint arises in the context of control: our ultimate goal is to simulate the interaction of localized arc filament plasma actuators (LAFFPAs) in a STBLI in conjunction with experiments being performed at the OSU Gas Dynamics and Turbulence Lab (GDTL).^{16,17} Control techniques generate their own coherent structures, whose impact on the naturally arising structures is crucial to develop a complete theory of control dynamics. For example, the effect of streamwise vortices generated by plasma-based control techniques on wall and free shear layers has been discussed extensively in Refs. 18 and 19. For such studies, it is critical that the upstream boundary layer possess the proper coherent structures expected in a spatially developing boundary layer. The most common approach to obtain such a layer from a bypass transition process is the blowing suction method,²⁰ in which zero net mass perturbations are added at a combination of frequencies.

In Refs. 21–23, we propose an alternate method of employing a steady counterflow force field to generate a disturbance that enhances transition to turbulence. A major property of the approach is that the tripping produces no artificial time scales into the process. Exhaustive comparisons with the literature indicate that the method reproduces all anticipated features of the boundary layer, including hairpin structures and near wall streaks, with no signature of the tripping mechanism.

A key observation of these studies was that finer meshes required a shorter domain to obtain the desired

turbulent boundary layer. In an effort to reduce the transition distance on coarser meshes that could otherwise support the equilibrium layer, the effects of varying some of the parameters in the force field were examined in Ref. 22. A stronger force field was found to yield a laminar profile with an adiabatic wall condition. Fixing the temperature at the turbulent adiabatic wall temperature recovered the desired profile within a shorter distance than for lower force fields. Hotter walls were also shown to provide a clean turbulent boundary layer.

In the present paper, we extend the approach to recover an adiabatic turbulent boundary layer with higher force field conditions. Additionally, we demonstrate that fine tuning of the parameters can be performed on a smaller upstream segment only. The properties of the recovering boundary layer after force field induced separation, in particular the structure of the generalized inflection point, correlate well with the subsequent evolution of the boundary layer profile.

In the second part of the paper, we discuss the STBLI itself. An oblique shock (generated from a 9° wedge angle) is allowed to interact with the generated equilibrium turbulent boundary layer ($M = 2.33$, $Re_\theta = 3048$), which corresponds to the experiment of Ref. 17 with a reduced Reynolds number to allow access to LES. The mean features of the interaction (interaction and separation bubble length) are shown to scale with the incoming boundary layer thickness, which allows comparison between the computation and experimental data. Many aspects of the interaction are examined including mean and instantaneous skin friction, velocity profiles (compared to experimental PIV data), and surface pressure. Particular emphasis is placed on the unsteady aspects of the STBLI. The amplification and change in character of the turbulence within the boundary layer is examined in several different ways, demonstrating that the interaction causes a significant departure from equilibrium, which relaxes downstream. The low frequency oscillations of the surface pressure that have been observed in previous computations over a range of conditions are confirmed, and are shown to match those of the experimental data. Analysis of the length scales of coherent structures shows that the interaction causes first a reduction and then an expansion of the structures.

The final case that we examine is the control of the STBLI by the use of the aforementioned LAFPA actuators, which are modeled as a thermal bump. These thermal bumps are pulsed at a frequency consistent with the peak frequency of the surface pressure fluctuations near the reattachment point. Examination of the results of this simulation indicate that the control mechanism is causing a reduction in the length of the separated region, and that for the current control parameters this is being achieved through a localized heating effect. Ongoing simulations are being conducted to determine the effects of variation of the thermal bump temperature and pulsing frequency, and to determine the effect of the actuator on the unsteadiness of the STBLI.

This paper is structured as follows. The theoretical and numerical models, including the tripping mechanism are detailed in Sec. II. Section III contains information about the particular flow conditions, tripping parameters, and grids. Results are presented and discussed in Sec. IV, with turbulent boundary layer generation given in Sec. IV.A, the baseline STBLI in Sec. IV.B, and the preliminary control investigation in Sec. IV.C. Finally the conclusions that can be drawn from these results are provided in Sec. V.

II. Theoretical and Numerical Model

The flows of interest in this study are governed by the full compressible Navier-Stokes equations supplemented by source terms for the interaction of the force field that trips the flow. Details of the governing equations are provided in Refs. 21,23. To describe the properties of the trip however, we provide a summary. The governing equations can be written in flux vector form as:

$$\frac{\partial \mathbf{U}}{\partial t} + \frac{\partial \mathbf{F}_I}{\partial x} + \frac{\partial \mathbf{G}_I}{\partial y} + \frac{\partial \mathbf{H}_I}{\partial z} = \frac{\partial \mathbf{F}_V}{\partial x} + \frac{\partial \mathbf{G}_V}{\partial y} + \frac{\partial \mathbf{H}_V}{\partial z} + \mathbf{S} \quad (1)$$

where \mathbf{U} is the solution vector, $\mathbf{U} = [\rho, \rho u, \rho v, \rho w, \rho e_T]^T$, \mathbf{F}_I etc. contain inviscid terms, \mathbf{F}_V etc. contain the viscous effects. \mathbf{S} contains the force field source terms. As discussed in Ref. 24 the force field is loosely modeled after the mean value obtained in Alternating Current Dielectric Barrier Discharges (AC-DBDs). The ratio of electrical to inertial forces, D_c

$$D_c = \frac{\rho_{c,ref} e_c E_{ref} L_{ref}}{\rho_{ref} U_{ref}^2}, \quad (2)$$

is employed to specify the strength of the force field:

$$\mathbf{F}_e = D_c \theta \varepsilon \alpha \rho_c \mathbf{E} \delta_{cr}, \quad (3)$$

whose magnitude is assumed to vary linearly by:

$$|\mathbf{E}| = E_0 + \frac{1 - E_0}{b}x + \frac{1 - E_0}{a}y, \quad (4)$$

where $E_0 = V_e/d$ (V_e is the applied voltage and d is the stream-wise distance between the two electrodes). Figure 1 shows the typical location and size of the DBD relative to the computational domain, and also an enlarged region near the DBD that shows the force vectors and region of application. Details of the specific choices for the parameters in the model are presented later.

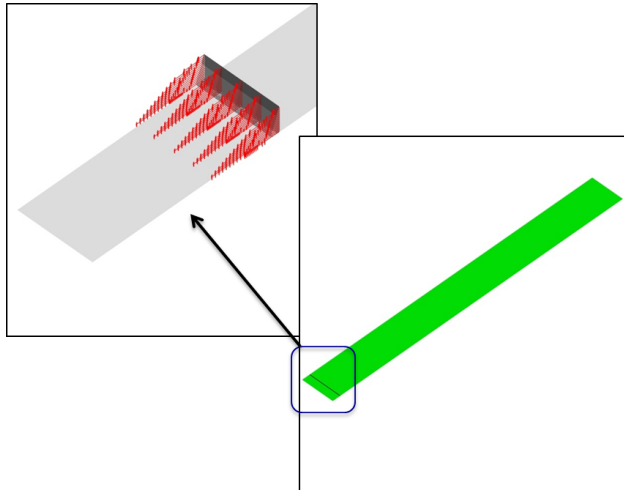


Figure 1: Schematic showing the relative size of the DBD actuator to the domain and the orientation and relative magnitude of the applied force field.

The STBLI simulations are performed on the same mesh as the upstream procedure *i.e.* the spatially developing boundary layer is simulated at the same time as the STBLI. The code used, FDL3DI, was developed at the Air Force Research Lab (AFRL)²⁵ and contains options for several different spatial schemes including high-order compact schemes, and the second order Roe scheme using MUSCL. In this work, we invoke a recently developed fifth order bandwidth and order optimized WENO scheme with Roe fluxes (see Ref. 26 for the inviscid fluxes, together with a sixth order compact scheme for the viscous fluxes. The time integration is performed with the implicit Beam-Warming scheme using two sub-iterations and approximate factorization. This method may be characterized as an implicit LES (*i.e.* ILES) in which no explicit sub-grid model is used.

III. Simulation Parameters

Table 1 shows the flow conditions of the STBLI experiments that have been run at the Ohio State University GDTL.¹⁷ Similar to the work of other researchers, Refs. 12, 27 etc., the computations operate at a Reynolds number that is much smaller (1/10) of the experiment to make the problem accessible to computations; the second column shows the modified conditions. Since the separation length scales on the order of δ , we maintain $U_\infty \delta$, and the Mach number, to be similar to those in experiment, so that the low frequency phenomena of interest (which scale as freestream velocity and separation length³ are captured); to lower the Reynolds number the pressure and density were reduced by a factor of 10. Note that the wall temperature listed is the laminar adiabatic wall temperature (its variation is discussed below). The OSU STBLI experiments had an adjustable angle for the shock-generating wedge, with angles of 7°, 8° and 9°.

In this paper, the strongest shock case ($\theta = 9^\circ$) is simulated. The properties of this oblique shock are found in Table 2.

To initiate the upstream boundary layer generation profile, a laminar boundary layer profile, calculated using a compressible Blasius solution with the thickness listed in Table 1, is used as an inflow boundary condition and an initial condition for all interior points. No-slip wall boundary conditions were imposed at the wall. For the y_{max} and x_{max} boundary conditions the value is extrapolated from the interior value. Periodic boundary conditions are used for the span-wise (z) direction. The flow was allowed to develop for several flow through times as the boundary layer was sampled for statistical and mean properties. For the STBLI, the y_{max} boundary condition was changed such that for $x < x_{shock}$ the pre-shock conditions are specified, and for $x \geq x_{shock}$ the post-shock conditions are specified. For the given grid, $x_{shock} = 21.44$, which provides an inviscid shock reflection point of $x = 60.0$.

A schematic of the grid is shown in Fig. 2. The Δx values divide the grid into five sections: an inflow section where the grid refines, a constant spacing region centered on the DBD actuator, a coarsening section, another constant spacing section, and then a final coarsening at the outflow. The Δy values of the grid consist of a $tanh$ expansion of the spacing starting with a specified Δy at the surface, and transitioning to a power-law variation at the incoming boundary layer height. The Δz values of the grid are constant at all span-wise locations. A brief overview (see Sec. IV.A) of the turbulent boundary layer properties is given for the A and C grids listed in Table 3. The STBLI (Secs. IV.B and IV.C) is simulated on the coarsest grid (C, ~ 20 million grid points).

For all simulations the center of the trip is fixed at $x = 2.6\delta_{99,0}$ (the $\delta_{99,0}$ will be dropped from further discussions of coordinates) downstream of the leading edge, with the size of the force field triangle fixed to $a = 0.03125$ (height), and $b = 0.125$ (length). The forcefield is oriented in an upstream (counter to the flow) direction. The tunable parameters are D_c , and the wall thermal condition, whose optimal values have been explored in Ref. 22 and will be further discussed in Sec. IV.A.1.

The tunable parameters for the tripping mechanism for the fine grid given in Ref. 21 are $a = 0.03125$, $b = 0.125$, and $D_c = 12.5$. Details of the parameter choice for the coarse grid are noted in Ref. 22, where we extended the tripping method by enabling energy interactions and modifying the wall thermal boundary condition from adiabatic to a constant value. By these modifications we were able to achieve results consistent with the finest grid on the coarse grid using $D_c = 25.0$, and $T_w = 1.95$ (which is the adiabatic wall temperature for the turbulent wall region).

The implicit time scheme that is implemented within FLD3DI allows for relatively large time steps. The boundary layer development and baseline shock cases were run with $\Delta t^* = 0.001$, which corresponds to a physical $\Delta t = 9.5 \times 10^{-9}$ s.

Table 1: OSU Flow Conditions.

Property	Experimental	LES
M_∞	2.33	2.33
U_∞ (m/s)	556	556
P_∞ (Pa)	23511.12	2351.11
T_0 (K)	295.6	295.6
T_w (K)	269.75	269.75
$\delta_{99,0}$ (m)	5.3×10^{-3}	5.3×10^{-3}
θ (m)	7.68×10^{-4}	7.68×10^{-4}
Re_δ	175202.06	17520.21
Re_θ	25387.77	2538.78

Table 2: Oblique shock properties.

Property	value
θ	9°
M_1	2.33
β	32.96°
M_2	1.98
p_2/p_1	1.71
ρ_2/ρ_1	1.46

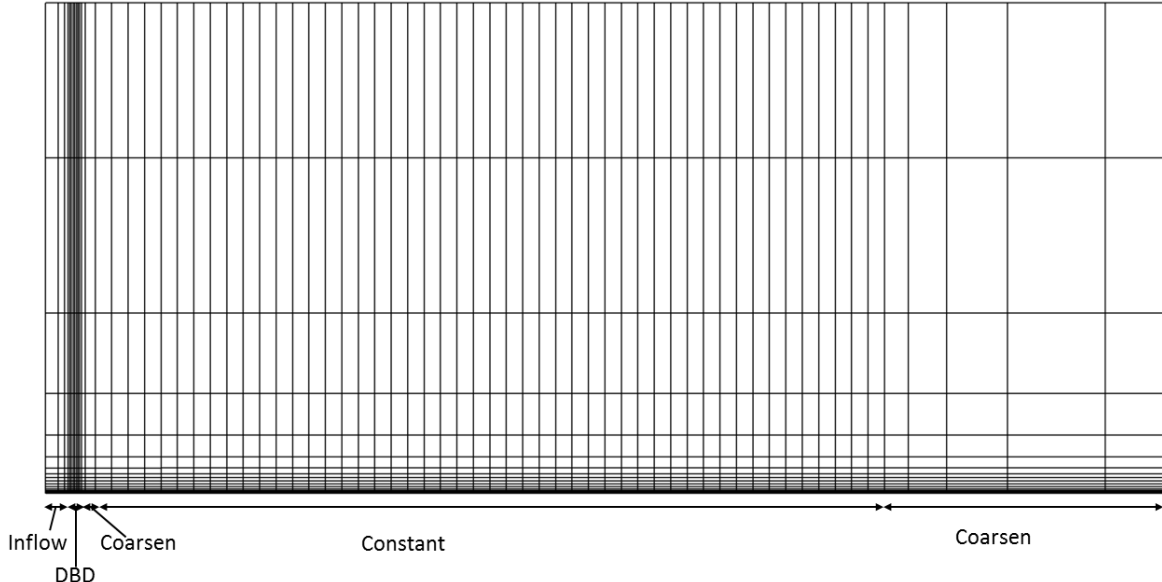
Figure 2: Schematic of the grid showing the different Δx regions and the clustering of y values near the wall.

Table 3: Properties of meshes employed for upstream boundary layer generation and STBLI.

	A	B	C
$X \times Y \times Z$	$95 \times 25 \times 5$	$95 \times 25 \times 5$	$95 \times 25 \times 5$
$N_x \times N_y \times N_z$	$1301 \times 251 \times 201$	$1101 \times 201 \times 167$	$917 \times 167 \times 133$
N_{total}	6.564×10^7	3.696×10^7	2.025×10^7
$N_{x,dbd}$	100	100	100
$X_{dbd,center}$	2.6	2.6	2.6
$X_{dbd,length}$	1.0	1.0	1.0
Δx_{dbd}	0.010	0.010	0.010
$N_{x,constant}$	1000	833	666
$X_{constant,start}$	4.10	4.50	4.62
$X_{constant,length}$	66.5	70.5	66.4
$\Delta x_{constant}$	0.0665	0.0846	0.0997
$\Delta x_{constant}^+ (x = 65)$	16.35	20.55	23.51
$N_{y,bl}$	151	125	101
Δy_{wall}	1.96×10^{-3}	1.96×10^{-3}	1.96×10^{-3}
$\Delta y_{wall}^+ (x = 65)$	0.4822	0.47641	0.4621
Δy_{bl}	0.0110	0.0151	0.0204
Δy_{max}	1.090	1.427	1.543
Δz	0.0250	0.0299	0.0376
$\Delta z^+ (x = 65)$	6.15	7.26	8.86

Table 4: Boundary Layer Tripping Test Cases.

Name	Flow	Grid	D_c	T_w	x_{aw}
A_12.5_aw	OSU	A	12.5	T_{aw}	
B_12.5_aw	OSU	B	12.5	T_{aw}	
C_12.5_aw	OSU	C	12.5	T_{aw}	
C_25_aw	OSU	C	25	T_{aw}	
C_25_1.95	OSU	C	25	1.95	
C_25_2.5	OSU	C	25	2.5	
C_25_1.95x15	OSU	C	25	1.95	15
$M = 2.92$ short	HIFIRE-1	A, $x \leq 15$	25	2.44	7.5
$M = 2.92$ full	HIFIRE-1	A	25	2.44	7.5

IV. Results and Discussion

IV.A. Upstream Turbulent Boundary Layer Profile

As noted earlier, the procedure to obtain the upstream equilibrium boundary layer profile forms a crucial part of the STBLI simulation. We first summarize the procedure as developed in Refs. 21–23, followed by new results that further improve the method to provide a highly versatile approach.

Table 4 shows the different cases that will be discussed. Results from the first six cases were described in Ref. 22, and are summarized below. The name of the case reflects the mesh size, the value of D_c , and the wall thermal condition, which has a significant impact in the development of the boundary layer in this compressible case. For example $A_12.5_aw$ represents a solution on mesh A with $D_c = 12.5$, and an adiabatic wall condition, while $C_25_1.95$ represents a solution on mesh C with $D_c = 25$, and a wall temperature fixed at $T_w/T_\infty = 1.95$. condition. The last three cases are motivated by the need to streamline the procedure: the notation for these is explained in Section IV.A.1.

Simulations presented in previous work,^{21,23} showed that a more rapid tripping of the boundary layer results in the need for smaller meshes. However, a simple increase in D_c yields a stronger initial separation region, but ultimately provides a laminar solution downstream. To test the hypothesis that the transition procedure is sensitive to the wall thermal condition, several simulations with fixed wall temperature were performed,²² and it was shown that an equilibrium boundary layer could be recovered. A summary of these results is now presented for cases $A_12.5_aw$ and $C_25_1.95$.

Figure 3 shows the stream-wise variation of the different measures of boundary layer thickness. Note that the mesh, all thermal condition, and D_c . However, the results are essentially independent of these parameters. The boundary layer maintains approximately constant thickness until it interacts with the DBD actuator at $x = 2.6$ producing a sharp localized decrease in δ_{99} , followed by a nearly constant boundary layer thickness until $x \sim 25.0$, after which the boundary layer begins to grow as the flow transitions. The displacement thickness δ^* and momentum thickness θ exhibit similar behavior. Within the fully turbulent region ($x \geq 50$), the shape factor $H = \frac{\delta^*}{\theta}$ lies within the values ($H \sim 1.4$) shown in Ref. 28 for $3500 \leq Re_\theta \leq 3800$.

For the current simulations, the incoming laminar boundary layer has a thickness equal to the desired $\delta_{99,0}$. The increase in δ_{99} subsequent to transition is almost linear — a similar effect is observed at the higher Mach number tested below. This facilitates a good estimate of the initial thickness required.

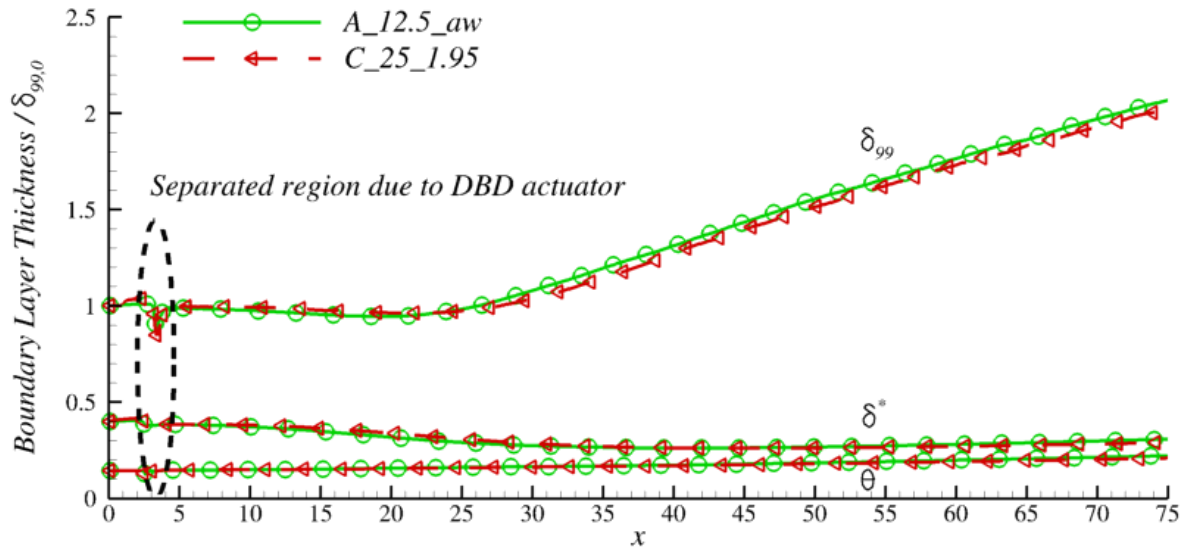


Figure 3: Boundary layer thickness without shock

Profiles of the law of the wall, shown in Fig. 4, where the velocity is transformed into an equivalent non-dimensional incompressible velocity using the Van Driest transformation (see Ref. 29) with the recovery factor $r = 0.89$. This shows that the profile is the expected turbulent boundary layer profile for $50.0 \leq x \leq 60.0$, which is the region in which the shock boundary layer interaction will be imposed.

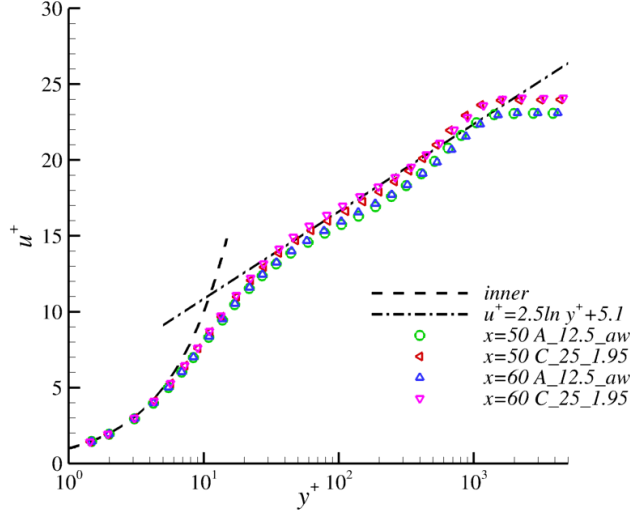


Figure 4: **Velocity profiles in Van Driest transformed coordinates at various stream-wise locations**

The density scaled Reynolds stresses, normalized by the shear velocity are given by:

$$R_{ij}^* = \frac{\bar{\rho} u'_i u'_j}{\bar{\rho}_w u_\tau^2}. \quad (5)$$

Figure 5a shows the normal Reynolds stresses at $x = 62.5$ with trend lines for the log law layer, labeled P-L, given by Perry and Li.³⁰ The numerical solution qualitatively follows the expected trendlines. Figure 5b examines the components of the shear stress, with the viscous shear stress normalized by:

$$\bar{\tau} = \frac{\bar{\rho} \bar{\mu} \frac{\partial \bar{u}}{\partial y}}{\bar{\rho}_w u_\tau^2}. \quad (6)$$

The total stress remains approximately equal to the wall value for $y^+ \leq 1000$: near the wall, the viscous shear makes up most of the stress, as expected from theory, and as distance from the wall increases the Reynolds shear stress R_{12}^* increases until it dominates, and then remains nearly constant in the log law region.

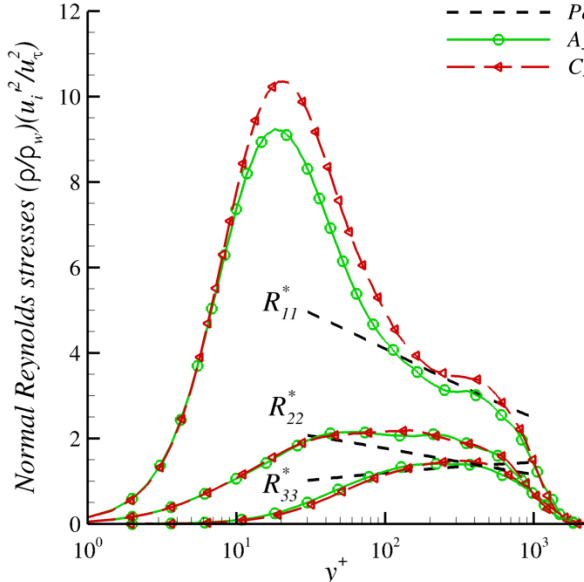
As noted earlier, a major factor in the development of the technique for spatially developing boundary layers are coherent structures. In the present case, these are implicitly reflected in auto- and two-point correlations.

Several different sets of two point correlations were provided in Refs. 21,22. As an example, an averaged two point auto-correlation function can be calculated using a formula given by Pirozzoli et al.:²⁰

$$C_{\alpha\alpha}(r_i = k_r \Delta x_i) = \sum_{k=1}^{N_i-1} \overline{\alpha_k \alpha_{k+k_r}}, \quad (7)$$

$$k_r = 0, 1, \dots, N_i - 1$$

where N_i is the number of grid points in direction i . (Note that the Eq. 7 is only applicable in regions with constant Δx_i .) The width of these correlations provide an estimate of the span-wise size of the largest



(a) Normal Reynolds Stress

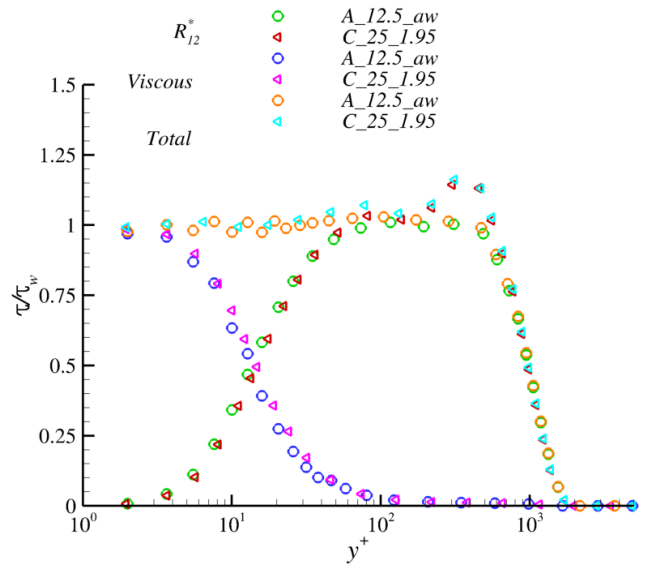


Figure 5: Density scaled stresses vs. distance from the wall at $x = 62.5$.

turbulent eddies. Figure 6a shows the correlation of the u -velocity fluctuations at various distances from the wall relative to the boundary layer thickness at $x = 62.5$, which demonstrates the growth of the largest eddies as the distance from the wall increases. Figure 6b shows a comparison between the correlations of each primitive flow variable for case $A_12.5_aw$; this shows that the domain is large enough in the span-wise direction such that the fluctuations in the center are not correlated with those near the periodic boundary.

A one-dimensional energy spectra of the streamwise velocity fluctuations can then be found from:²⁰

$$E_{uu} \left(k_i = \frac{n}{N_i-1} \frac{1}{\Delta x_i} \right) = 1 + 2 \sum_{k_r=1}^{(N_i-1)/2} C_{uu} (k_r \Delta x_i) \cos \left(\frac{2\pi n k_r}{N_i-1} \right) . \quad (8)$$

n = 0, 1, ..., (N_i-1)/2

Figure 7 shows the one-dimensional energy spectra for *u-velocity* fluctuations in the span- and streamwise directions within the log law region ($y^+ = 116$), again at $x = 62.5$, which demonstrates that there are no spurious length scales introduced by the simulated DBD actuator. The spectra also show a $k^{-5/3}$ rolloff at higher wave numbers, as expected from theory.

The development of turbulence is accompanied by the generation, evolution and transport of coherent structures. Isosurfaces of Q-criterion ($Q = 0.5$) colored by the u-velocity are shown in Fig. 8. A vortex generated by the DBD appears at the lower left hand corner of the figure. This is followed by a region of relatively few structures. Subsequently however, coherent structures appear in a sporadic manner along the span and finally there is a rapid break down into fully developed turbulence. As can be seen in both the fine and coarse grid cases the structures are hairpin vortices that begin near the wall, and are inclined in the streamwise direction.

IV.A.1. Investigation of tripping properties

We now generalize the method to recover adiabatic wall profiles at the higher D_c , generate insight into methods to determine the size of the parameter and finally demonstrate application to a higher Mach number case.

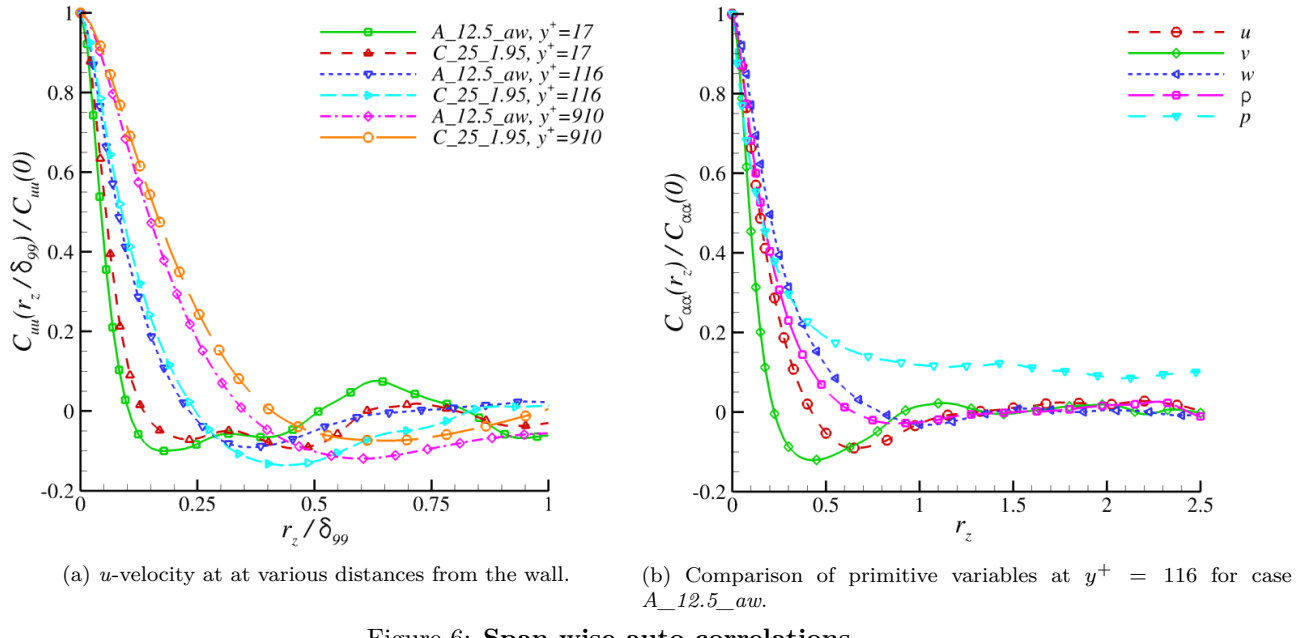


Figure 6: Span-wise auto-correlations

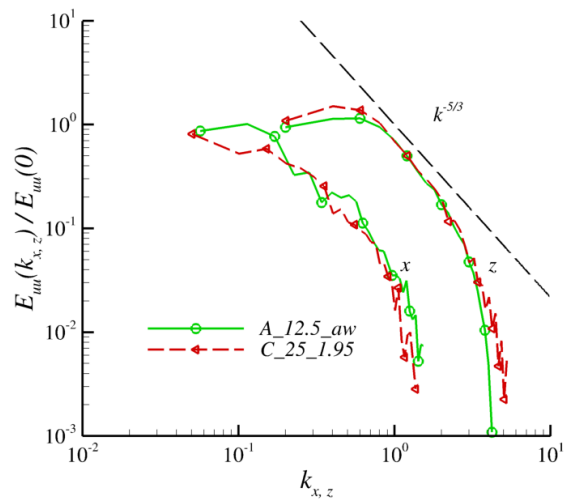


Figure 7: One-dimensional energy spectra at $x = 62.5$.

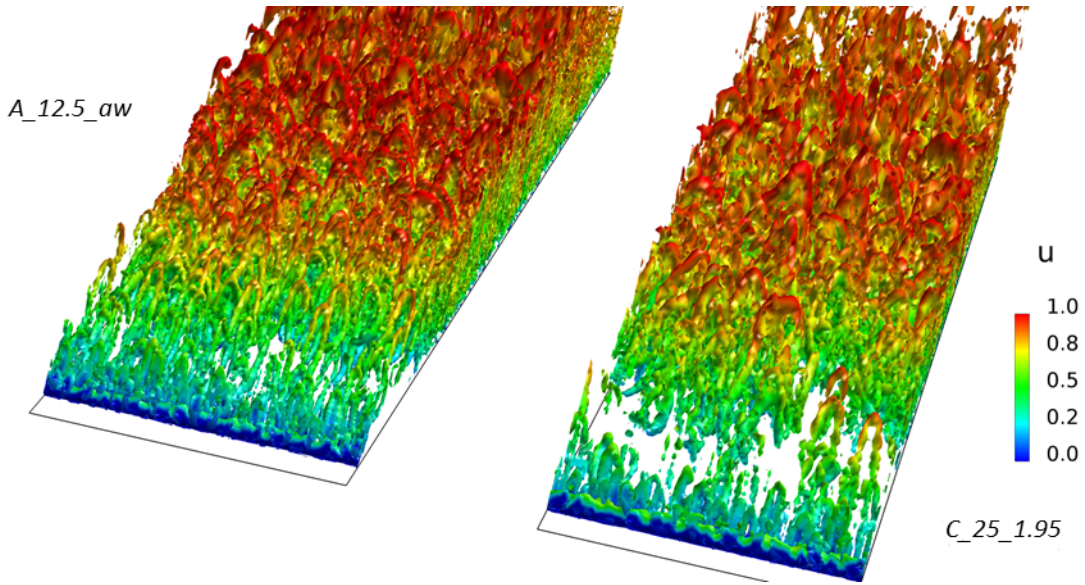


Figure 8: $Q = 0.5$ isosurfaces colored by u -velocity

As noted above, using the original tripping parameters ($D_c = 12.5$) with an adiabatic wall on the coarsest grid provides the required turbulent boundary layer after a relatively delayed transition, which limits the usefulness for the full STBLI studies (a significantly lengthened domain would be required). An increase of the tripping strength to $D_c = 25.0$ without an adjustment to the wall thermal boundary condition, yields a flow that re-laminarizes downstream of the trip. Use of an isothermal wall boundary condition at both $T_w/T_\infty = 1.95$ and $T_w/T_\infty = 2.5$ yields an equilibrium turbulent boundary layer, with the former achieving results consistent with the fine and medium grid cases in approximately the same transition length.

Two key questions have arisen from this analysis of the tripping mechanism. First, under what conditions will the boundary layer trip into turbulence and can these conditions be determined without solving the entire problem? Second, how can one obtain an equilibrium profile for an adiabatic wall condition instead of an isothermal condition on a less expensive grid? The answers to these questions will greatly simplify the choice of parameters for different Mach and Reynolds numbers.

We start by examining several properties of the boundary layer only simulations in the vicinity of the actuator trip to distinguish the tripping parameters that failed (i.e. the boundary layer laminarized) from those that succeeded. Figure 9 shows a comparison of the average properties near the flow for a selected set of cases. The first three ($A_{12.5_aw}$, $B_{12.5_aw}$ and $C_{12.5_aw}$) are those discussed originally in Ref. 21. The next case (C_{25_aw}), reflects the attempt to speed transition by increasing the force field while maintaining adiabatic wall temperature. The last two ($C_{25_1.95}$ and $C_{25_2.5}$) consider the higher D_c , with a wall temperature fixed at $T_w/T_\infty = 1.95$ (the adiabatic wall temperature in the equilibrium turbulent region), and $T_w/T_\infty = 2.5$ (a hot wall condition). For each of these cases in addition to the wall temperature, T_w (Fig. 9a), the boundary layer thickness Reynolds number evaluated with wall properties, $Re_{\delta_{99}}(\rho_w, T_w) = \frac{\rho_w U_\infty \delta_{99}}{\mu(T_w)}$ (Fig. 9b), and skin friction coefficient, c_f (Fig. 9c), are shown.

All cases show separation due to the counterflow force field as characterized by negative values of c_f , and the streamwise extent of separation region is approximately the same. However, the one case which laminarizes (C_{25_aw}) shows clearly different values and behavior in the wall temperature and Reynolds number figures. The wall temperature is significantly higher, and the recovery of $Re_{\delta_{99}}(\rho_w, T_w)$ is much more gradual, recovering to the value of the $C_{25_2.5}$ case after ~ 1.5 boundary layer thicknesses downstream of the trip. These parameters provide an initial indicator of the success or failure of the chosen actuator strength and thermal properties, and may indicate the existence of a critical $Re_{\delta_{99}}(\rho_w, T_w)$ below which the fluctuations are not able to amplify.

These average properties, however, do not permit a distinction between cause and effect. To explore further, we note that a key parameter is the stability of the region characterized by a separated shear layer

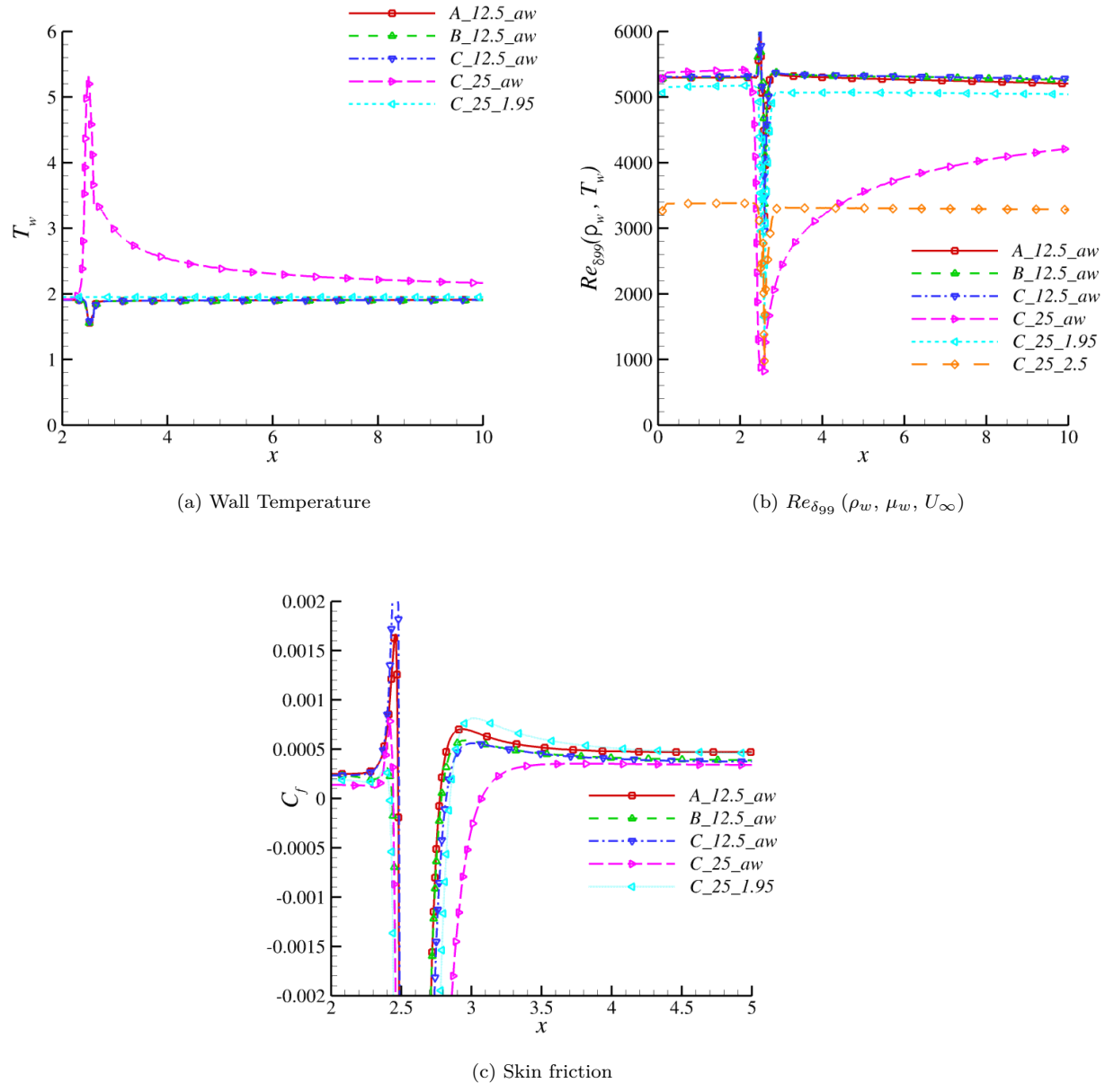


Figure 9: Average properties in the region of the trip

and subsequent development of the boundary layer after reattachment. Figure 10 examines the properties of the generalized inflection parameter (see Ref. 31):

$$\varphi = \frac{\partial}{\partial y} \left(\bar{\rho} \frac{\partial \bar{u}}{\partial y} \right), \quad (9)$$

at several stations along the length of the plate near the trip extending from upstream ($x = 1.1$), within ($x = 2.6$) and downstream of the trip ($x = 3.1$ and $x = 5.1$). Although all cases show separation, as observed in the c_f plot (Fig. 9c), the inflection point characteristics show substantial differences. Clear qualitative and quantitative differences are evident between the transitioning and laminarizing cases immediately downstream of the trip. Each of the turbulent cases has a significant negative peak immediately downstream of the separated region ($x = 3.1$), whose value diminishes with streamwise distance. The first zero crossing for all these cases occurs at $y \sim 0.09$ at $x = 3.1$ and $y \sim 0.2$ at $x = 5.1$. The unsuccessful simulation (*C_25_aw*) shows a very different behavior, with values being positive near the wall, going negative after the first crossing, until joining the other solutions. The region of greatest discrepancy between the curves occurs at the same maximum height of the separation bubble, $y \sim 0.08$.

These observations show that the characteristics of a successful turbulence are evident in the immediate vicinity of the tripping actuator. This suggests solutions to the two main issues, obtaining an adiabatic wall boundary layer profile with a higher D_c , as well as a quick method to test tripping parameters for new flow parameters.

To obtain a rapid method to determine the parameters, we consider the possibility of only simulating the region that encompasses the front part of the flow (i.e. a short distance downstream of the reattachment point) and testing the profiles obtained against the above features. If the flow shows the proper behavior, a full simulation would be warranted.

For the adiabatic wall condition, we consider the hypothesis that the wall thermal condition is only important in the regions near the tripping mechanism, and that a turbulent adiabatic wall condition can be obtained at a high D_c by maintaining a constant wall temperature for a small distance downstream and subsequently switching to adiabatic. Figure 11 shows this approach schematically.

Three simulations are performed to demonstrate the ability of the method to address both objectives, i.e. use only a short domain with generalized inflection point data to estimate proper parameters, and to obtain an adiabatic wall profile at higher D_c . The first is the same as *C_25_1.95*, except that the wall thermal condition is changed to adiabatic at $x = 15$, which is a significant distance downstream of the reattachment point (this case is referred to as *C_25_1.95_x15*). The second and third simulations consider a different set of parameters to establish the use of this method for different flight conditions; the parameters are taken upstream of the compression corner experiment of the HIFIRE-1 flight at a specific point in its flight path (as examined in Ref. 32 with RANS). These flight parameters are shown in Table 5; note that the Reynolds number has been reduced by a factor of 50 for the LES. For this set, one simulation (*M=2.92 short*) considers only up to $x = 15.0$ which is only 27% of the total number of grid points on the full domain. Based on successful completion of this less expensive simulation (i.e., the flow profiles are similar to those observed in Figs. 9 and 10), the full simulation (*M=2.92 full*) is then performed.

The generalized stability criterion for the three new cases is shown in Fig. 12, compared to a case that trips (*A_12.5_aw*) and one that does not (*C_25_aw*). The three new cases satisfy the behavior of a successfully tripping case (see Fig. 10). A detailed further analysis of the properties indicates that indeed, the obtained boundary layer satisfies both single and multi-point statistics of equilibrium turbulent boundary layers. Figure 13 shows selected properties of the turbulent boundary layer downstream for the two full domain cases including the Van Driest transformed velocity profiles (Fig. 13a, and the normalized Reynolds stresses (Fig. 13b). Clearly the conditions obtained are as expected and the method is successful.

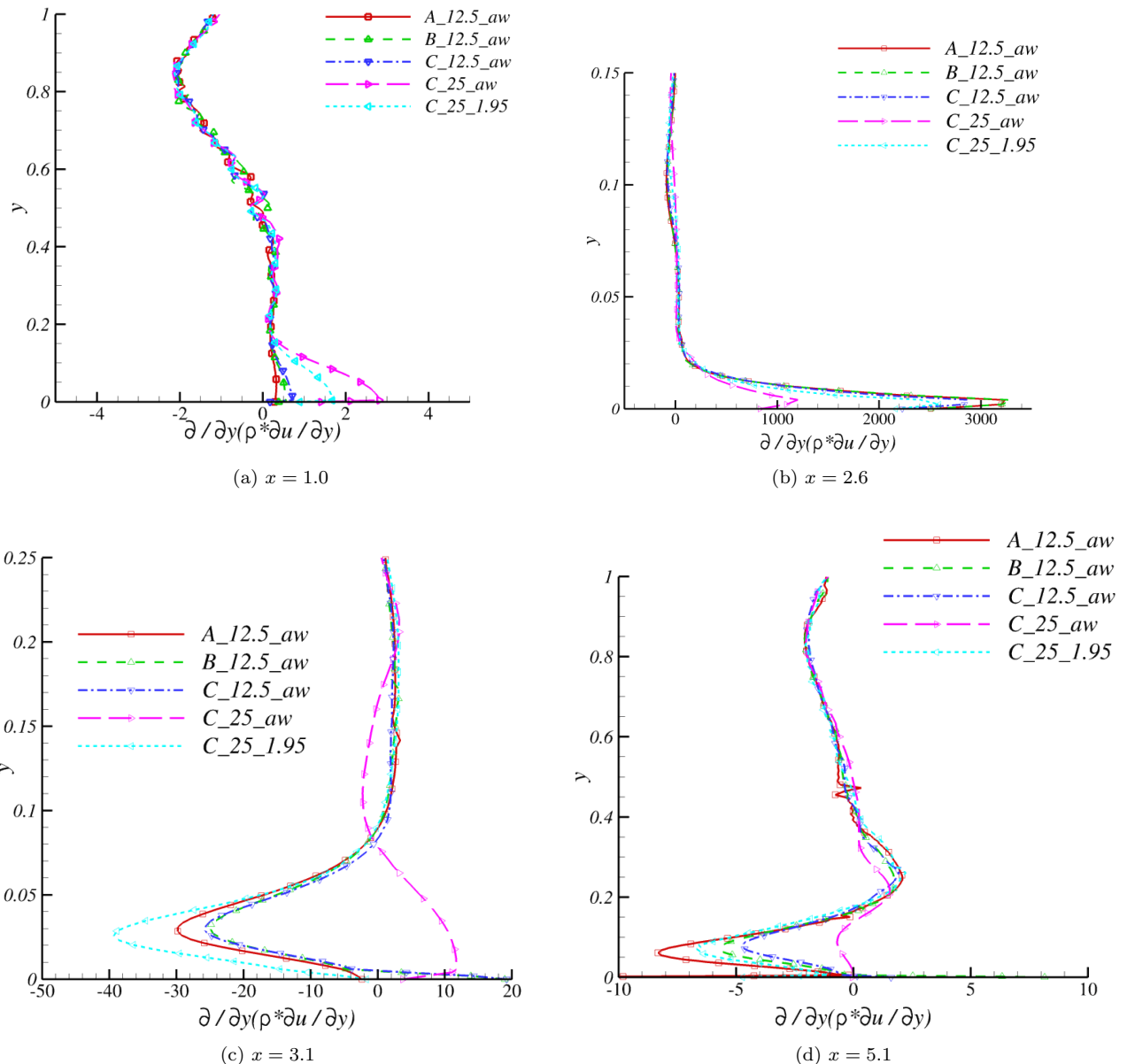


Figure 10: Generalized Stability Criterion

Table 5: HIFIRE-1 Flow Conditions.

Property	Experimental	LES
M_∞	2.92	2.92
U_∞ (m/s)	973.27	973.27
P_∞ (Pa)	68800	1376
T_0 (K)	746.18	746.18
T_w (K)	673.27	673.27
$\delta_{99,0}$ (m)	2.77×10^{-2}	2.77×10^{-2}
Re_δ	1352729	27054.6

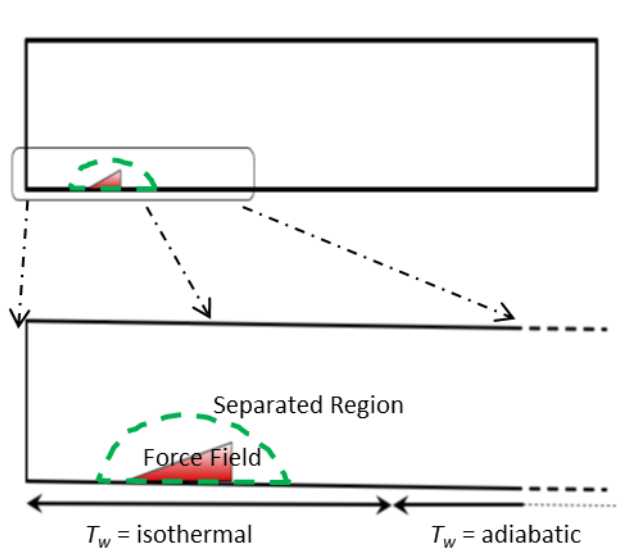


Figure 11: Schematic of Wall Thermal condition variation

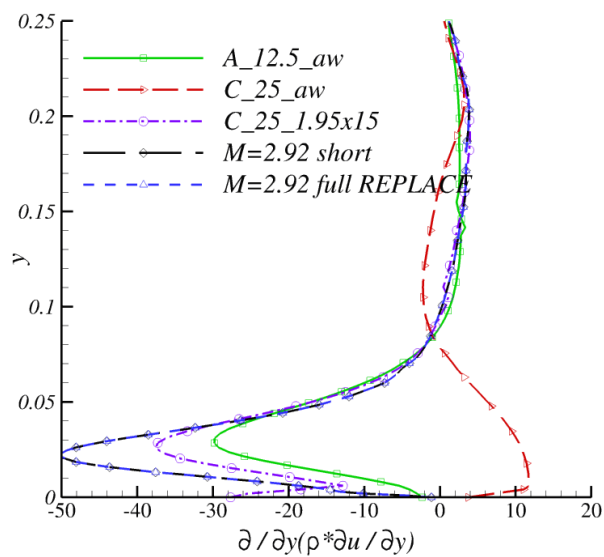


Figure 12: Generalized Stability Criterion for new cases at $x = 3.1$

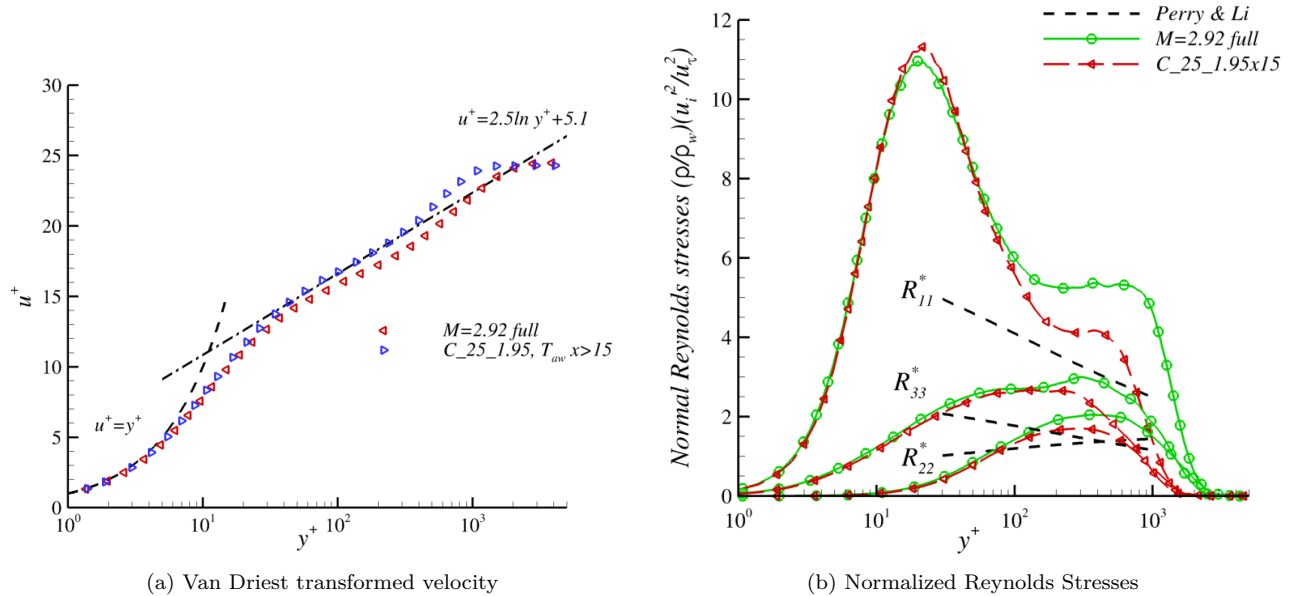


Figure 13: **Turbulent Boundary Layer Properties for new cases at $x = 62.5$ ($C_{25} \cdot 1.85$, $T_{aw} x > 15$) and $x = 50$ ($M=2.92 \text{ full}$)**

In summary, the actuator force based mechanism has been shown to effectively and efficiently yield equilibrium turbulent boundary layers for a variety of Mach and Reynolds numbers, as well as wall thermal conditions.

IV.B. Baseline STBLI

IV.B.1. Mean flow

Several important features of the mean flow are detailed in Fig. 14. The background shows contours of $|\nabla \rho|$, which highlights the location of the shocks and wave structures within the flow as well as the boundary layer thickness. An isosurface of $u = 0$ colored by pressure depicts the mean separated flow. An isosurface of $M = 1$ (colored purple) shows that prior to the interaction subsonic flow is only encountered near the surface, in the interaction region a peak in its extent is found near the shock reflection point, and downstream the height of the subsonic layer decreases towards the expected level for a supersonic boundary layer. Also labeled are the start of the interaction region $x = 53.73$ found by extrapolating the reflected shock to the surface, the mean separation location immediately after this at $x = 53.8178$, the mean reattachment location at $x = 57.9963$, and an “end” of the interaction region at the inviscid shock impingement point $x = 60$. This gives a dimensional interaction length of 33.23 mm ($6.182\delta_{99,0} = 4.07\delta_{99,x=50}$), which is approximately the incoming boundary layer thickness ($1.523 \times \delta_{99,0}$) times the experimental measurement of 21.81 mm . The mean separation bubble length is $4.1785\delta_{99,0} = 2.75\delta_{99,x=50}$, and the maximum height of the separation bubble is $0.033\delta_{99,0} = 0.022\delta_{99,x=50}$. The ratio of the separation length to the interaction length is within the range of values provided in Ref. 12.

The mean surface pressure is shown compared to the theoretical inviscid solution in Fig. 15 (note that unless otherwise specified the results are spanwise averaged). The pressure achieves 80% of its theoretical rise in the interaction region, and the remaining 20% occurs as the boundary layer relaxes. An instantaneous centerline pressure measurement is shown for comparison. The surface pressure does not show a plateau region as would be expected per Delery and Dussage,² but a similar lack of plateau has been reported in the LES solutions presented by Touber and Sandham,^{11,12,33} and the DNS of Pirozzoli and Grasso.¹⁰

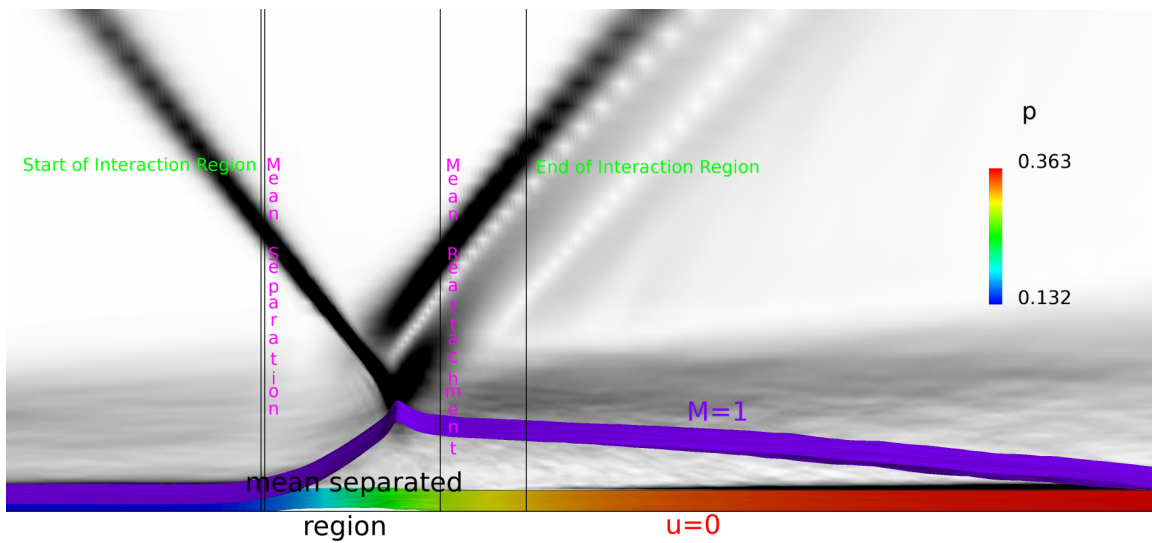


Figure 14: Overview of interaction showing mean shock locations, interaction and separation lengths, pressure rise and sonic line.

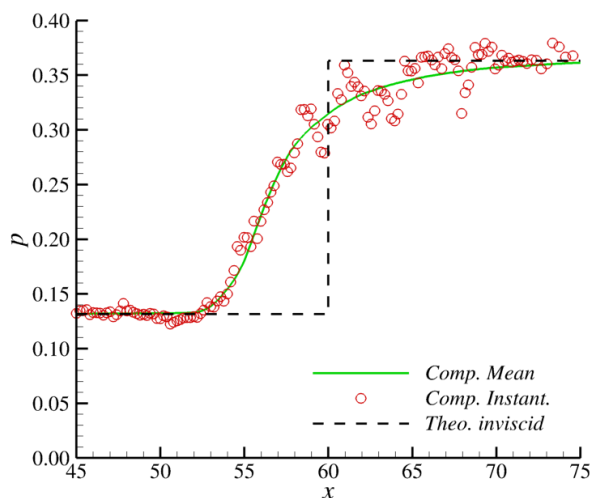


Figure 15: Mean surface pressure rise through the interaction.

The mean skin friction is shown along with the surface pressure in Fig. 16. The size of the mean separation region ($C_f \leq 0$) is shown relative to the interaction region. The separation begins only slightly downstream from the reflected shock foot. It can also be seen that the pressure begins to rise and skin friction drops before the defined start of the interaction region (extrapolated reflected shock foot location). The skin friction follows the same behavior of the pressure downstream of the interaction, trending back towards the expected behavior for an equilibrium turbulent boundary layer. Again this is consistent with the previously mentioned computational studies.

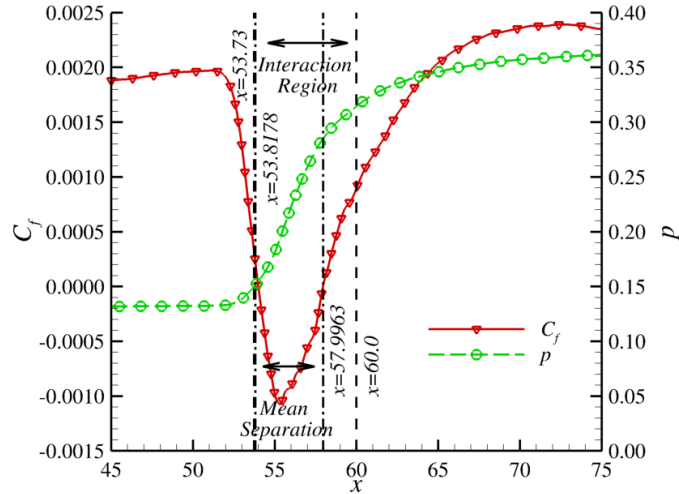
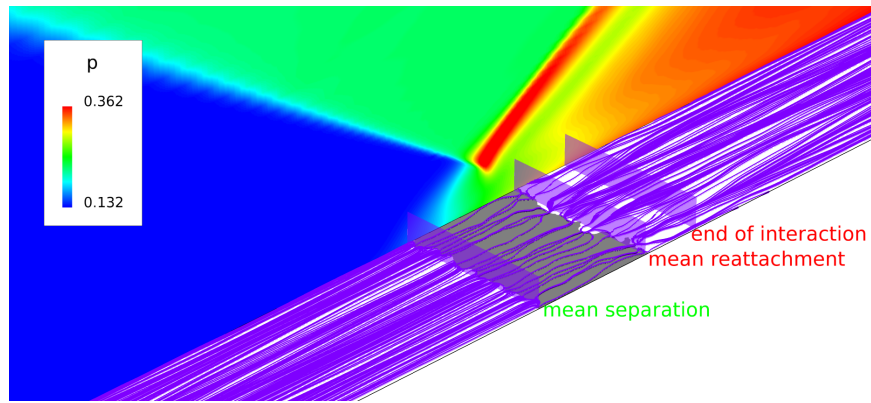


Figure 16: Skin friction and surface pressure within the interaction region.

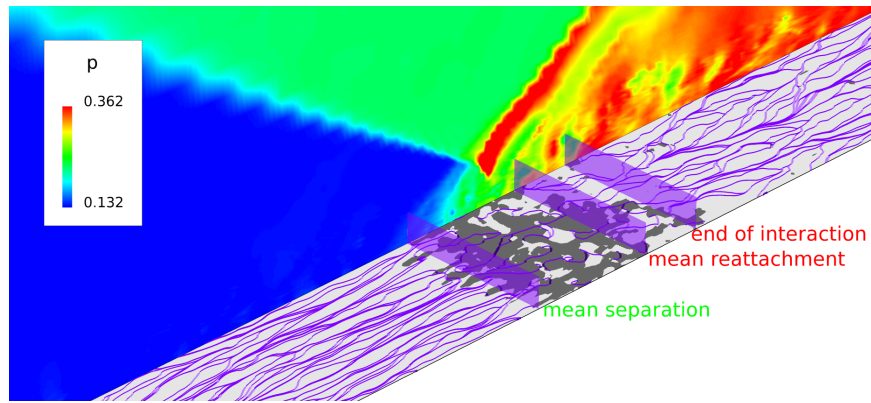
Figure 17 shows mean (Fig. 17a) and instantaneous (Fig. 17b) surface oil flows and separated regions. The background shows contours of pressure. The wall surface shows surface oil flow colored purple, and regions where the flow at the $j = 2$ plane has velocity less than zero which indicates separated flow colored dark gray. Also indicated are the mean separation and reattachment lines as well as the inviscid shock impingement point. The mean data shows a separation bubble with clear separation and reattachment lines. The instantaneous does not show a clear separation and reattachment, and in fact multiple separations and reattachments can occur on a line at a constant spanwise coordinate; lines of coalescence and divergence can be seen in both the mean and instantaneous data.

A comparison between an experimental Schlieren image and contours of $|\nabla \rho|$ from the computations is provided in Fig. 18. The Schlieren has been aligned with key points whose spatial location is known (such as the tip of the shock generator and its top surface), with coordinates non-dimensionalized by the experimental incoming δ_{99} . The computational result is scaled by the computational boundary layer thickness $\delta_{99,x^*=50.5}^* = 1.523$ taken just before the interaction, and the computational coordinate system is shifted such that zero lies at the location of the inviscid shock impingement point. A view that includes the full Schlieren with the known coordinate points is shown in Fig. 18a, and the region near the interaction is shown in Fig. 18b. As can be seen the key features such as shock locations and angles are matched. This demonstrates that the results scale spatially by the incoming boundary layer thickness and interaction length.

Figure 19 shows a comparison between three measures of boundary layer thickness for the boundary layer and STBLI simulations. The boundary layer thickness δ_{99} is growing as it approaches the interaction while momentum (θ) and displacement thicknesses (δ^*) remain nearly constant. Within the interaction region

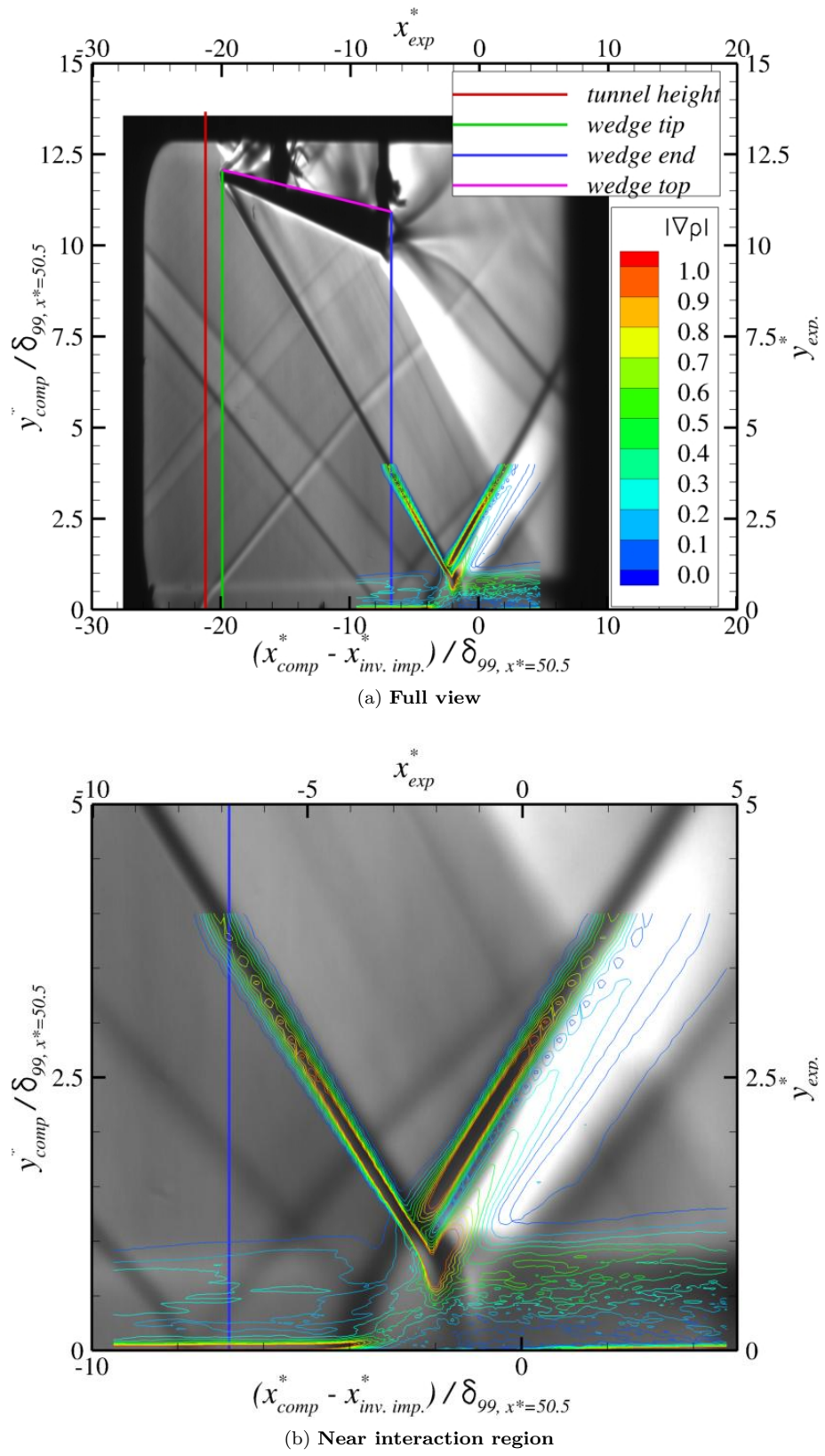


(a) Mean



(b) Instantaneous

Figure 17: Computed surface oil flow with pressure and separated regions.

Figure 18: Comparison of experimental Schlieren vs. computational $|\nabla \bar{\rho}|$.

the edge condition is not defined, so no thickness is reported. The edge velocity after the reflected shock is taken to be the freestream velocity after the theoretical inviscid reflected shock, and the decreased δ_{99} after the shock is due to the fact that the edge flow has not achieved its theoretical value (from which δ_{99} is calculated). The shape factor is modified from a value $H(x = 52) = 1.48$ before the interaction to $H(x = 60) = 2.09$, which recovers to $H(x = 75) = 1.58$ downstream of the interaction. The Reynolds number based on momentum thickness at $x = 50$ is $Re_\theta = 3048$, which has increased to $Re_\theta = 6750$ by $x = 70$.

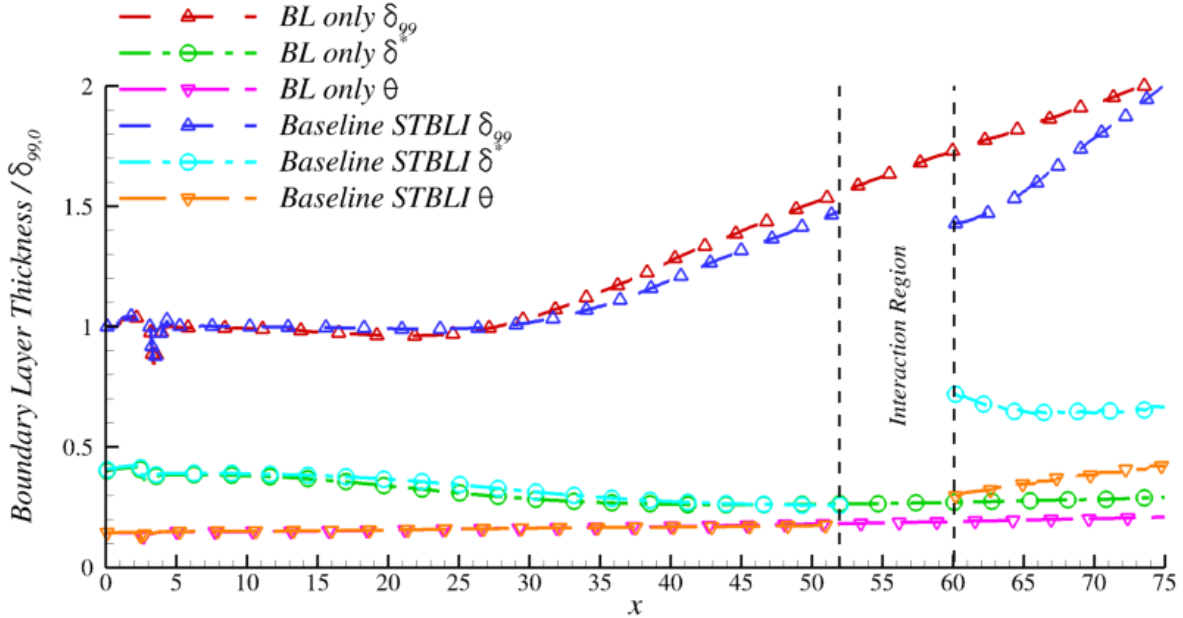


Figure 19: Comparisons of boundary layer thicknesses between the boundary layer and full STBLI simulations.

A comparison between the mean velocity components in the computations and the experiments are shown in Fig. 20. The experimental data (Figs. 20c & 20d) comes from the PIV of Ref. 17, and has been scaled such that the incoming boundary layer thickness, interaction length, and inviscid shock impingement point are matched (note that the experimental data has some errors due to contamination from surface oil flow measurements). As can be seen while not an exact quantitative comparison, the u - (Fig. 20a) and v -velocity (Fig. 20b) computational results both demonstrate the major features of the experiment, such as the shock reflection and the boundary layer thickening downstream of the interaction. However in the computational result the region with $u \leq 0.3$ represented by the blue contours are confined to a maximum distance from the wall of $y \sim 0.5$, whereas the experimental results shows them penetrating to a maximum height of $y \sim 1.0$, which indicates that the separation bubble height is larger in the experiment (even though no negative streamwise velocity was resolved by the PIV), which was also indicated in the LES of Ref. 33. The v -velocity contours in both the computations and experiment show a ∇ shape containing relatively high values that has its origin near the mean separation point, and its “top” inclined with the impinging shock; the experimental shows a higher positive velocity, which again is due to the larger height of the separated region.

Figure 21 shows mean u -velocity profiles at various streamwise locations. The lines labeled u_1 , u_2 , u_3 represent the theoretical inviscid incoming free stream, post impinging shock and post reflected shock values, which are 1.00, 0.907, and 0.825 respectively. A comparison between the experimental (extracted from the PIV data shown in Fig. 20 and represented by dashed lines) and computational profiles (solid lines) for three

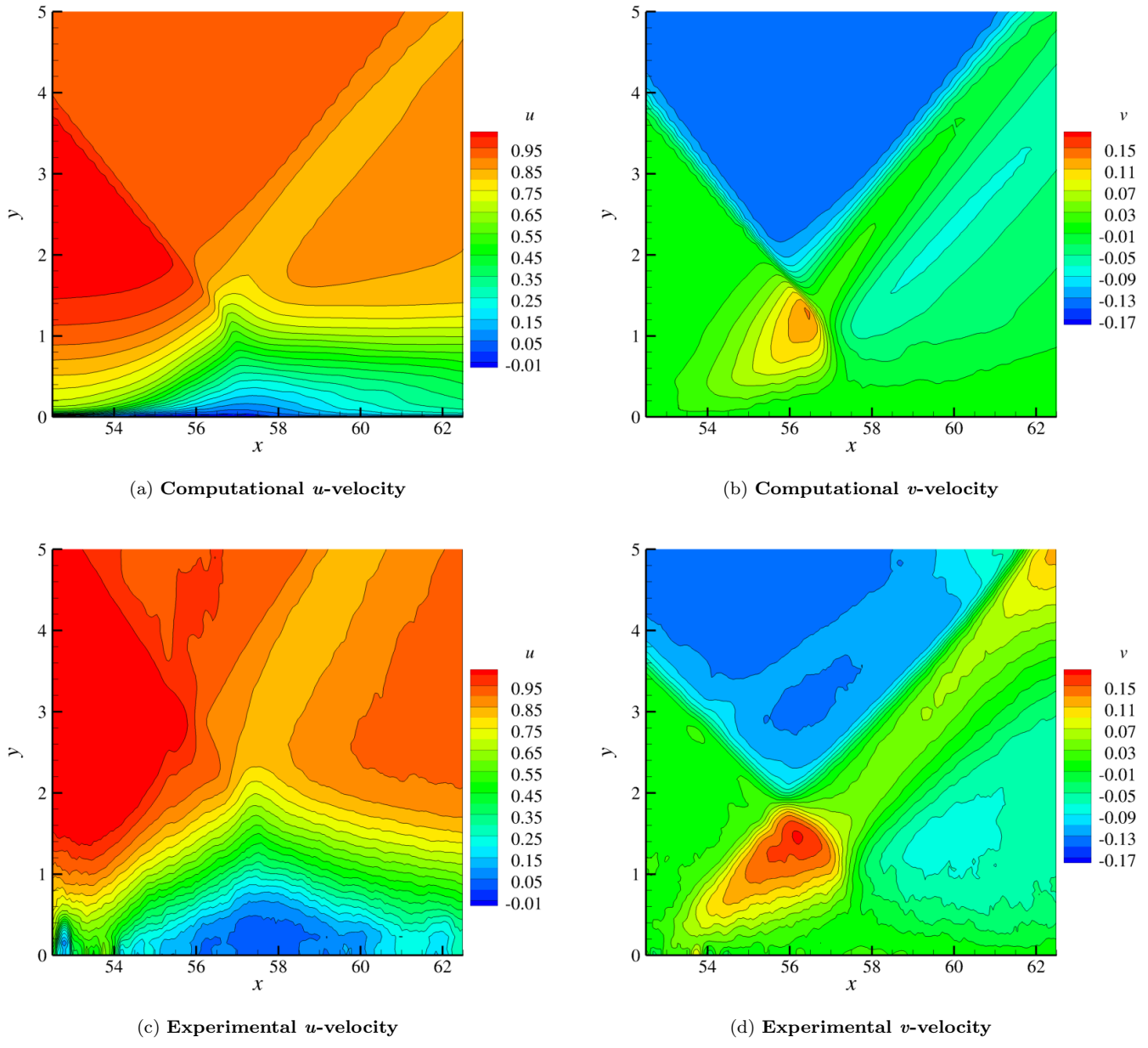
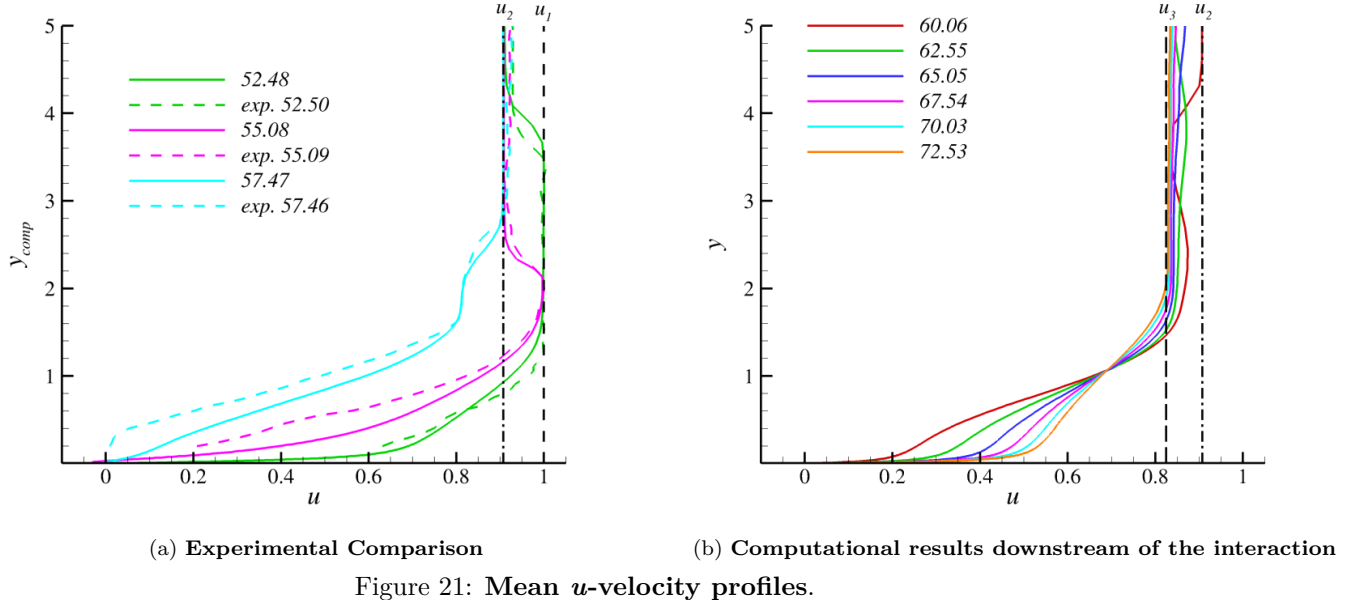


Figure 20: Mean velocity comparison between computations and experiment.

locations is provided in Fig. 21a. The profile just before the interaction ($x = 52.5$) shows good agreement, while the locations within the interaction ($x \sim 55, 57.5$) show good agreement away from the wall while they follow the same trends near the wall, which is again due to the discrepancy in separation bubble height. Selected profiles downstream of the interaction are given in Fig. 21b, and show that the flow is relaxing back towards the expected profile for flat plate boundary layer.



The evolution of the boundary layer from the classical equilibrium turbulent boundary layer through the interaction and its recovery back towards equilibrium can be seen in the Van Driest transformed velocity profiles shown in wall units in Fig. 22 for four streamwise locations. The incoming boundary layer at $x = 47.50$ follows the expected law of the wall behavior. Within the interaction at $x = 55.075$ a separated region can be clearly seen with no identifiable log law region and a large wake component. At the end of the interaction ($x = 60$), a small logarithmic region exists for $10 \lesssim y^+ \lesssim 65$, followed by a large wake region. The final profiles shows that the flow is trending towards the law of the wall, but that the wake region has been significantly increased, which is similar to the behavior shown in the DNS of Ref. 10.

IV.B.2. Flow statistics

The evolution of the Reynolds stresses at through the interaction are provided in Fig. 23. R_{11}^* (depicted in Fig. 23a) follows the expected behavior at $x = 47.60$, $x = 50.09$ with a peak of 11.85 at $y^+ \sim 22$. The profile begins to modify at $x = 52.58$ with a peak stress 15.55 at the same approximate y^+ as the previous locations, and the behavior for $y^+ \gtrsim 100$ remains the same. The peak stress increases at $x = 55.08$ (which is in the middle of the mean separated region) to 83.3 , at a $y^+ \sim 37$, and no longer follows the same trend for $y^+ \gtrsim 100$. Near the end of the separated region at $x = 57.57$ the peak has risen to 232.8 at a $y^+ \sim 106$. Just after the end of the interaction at $x = 55.08$, the peak has decreased to 62.2 at a $y^+ \sim 205$. As the flow continues away from the interaction, the stresses continue to decrease and are trending towards the pre-interaction profile, but continue to have an excess for $y^+ \gtrsim 100$. R_{22}^* (depicted in Fig. 23b) and R_{33}^* (depicted in Fig. 23c) follow the same general behavior. The wall normal and spanwise directions peak stresses are $\sim 30\times$ the value attained in the boundary layer prior to the interaction while the streamwise is $\sim 19\times$.

The Reynolds shear stress normalized by the wall viscous shear stress is shown in Fig. 23d. In the incoming boundary layer locations the peak stress is 1.9 at $y^+ = 266$. Within the interaction the peak stress

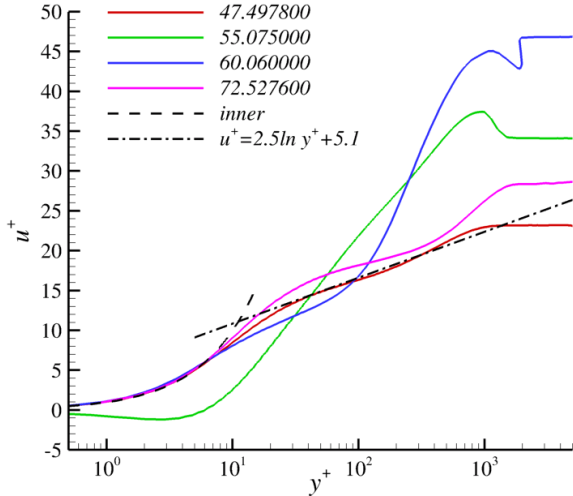


Figure 22: Streamwise velocity profiles in Van Driest transformed coordinates at various streamwise locations.

is amplified to 39.1 at a $y^+ = 72.2$. This corresponds to the previously mention amplification value for R_{11}^* . It also can be seen that the shear stress profiles shift closer to the wall.

The amplification of the turbulence is examined in Fig. 24. The turbulent kinetic energy ($k = \frac{1}{2} (\widetilde{u''u''} + \widetilde{v''v''} + \widetilde{w''w''})$, shown in Fig. 24a), shows that upstream profile has the expected behavior (seen previously in the context of the equilibrium turbulent boundary layer). In the initial part of the separated region ($x = 55.1$), there is a substantial (almost threefold) increase in k at a slightly higher location. The peak moves away from the wall as the streamwise location increases. The peak value attenuates to a level equivalent to the upstream profile, but the peak is at a much higher location reflecting the non-equilibrium state of the turbulent boundary layer. The turbulent shear stress profiles, $\tau_{xy} = -\widetilde{u''v''}$, (Fig. 24b) show again that the interaction amplifies the turbulence. In this case however, the increase first takes place near the wall which represents the increased diffusivity associated with the interaction. The values of the shear stress continue to increase with the peak moving away from the wall until slightly past reattachment and then begins to relax towards the expected equilibrium behavior. For completeness the structure parameter, defined as $\tau_{xy}/2k$ by Ref. 10, is provided in Fig. 24c. The form of the structure parameter remains similar upstream and downstream of the separation, however within the separated region there are major excursions. At $x = 55.1$ the k has a narrower peak, whereas the shear has been amplified over a much larger extent of the boundary layer height, which corresponds to the initial decrease in the structure parameter, near the wall followed by an increase farther away. At $x = 57.6$ the structure parameter is lower throughout.

In the experiments of Webb et al.¹⁷ surface pressure measurements were taken at several locations. In this computational study six of these locations along the centerline were chosen for comparison. The experimental locations were non-dimensionalized relative to the experimental interaction length with a zero point at the inviscid shock impingement location; the computational locations were chosen such that they had the same non-dimensional coordinates using the computational interaction length. Figure 25 shows the location of the computational measurements in relation to the mean skin friction coefficient and surface pressure; Table 6 provides the coordinates of each location.

The pressure fluctuations at these locations have been provided in Fig. 26. These signals have been passed through a lowpass filter with a cutoff frequency of $St \sim 0.25$ in order to highlight the low frequency content. The first three locations which include two locations outside of the interaction region and one point

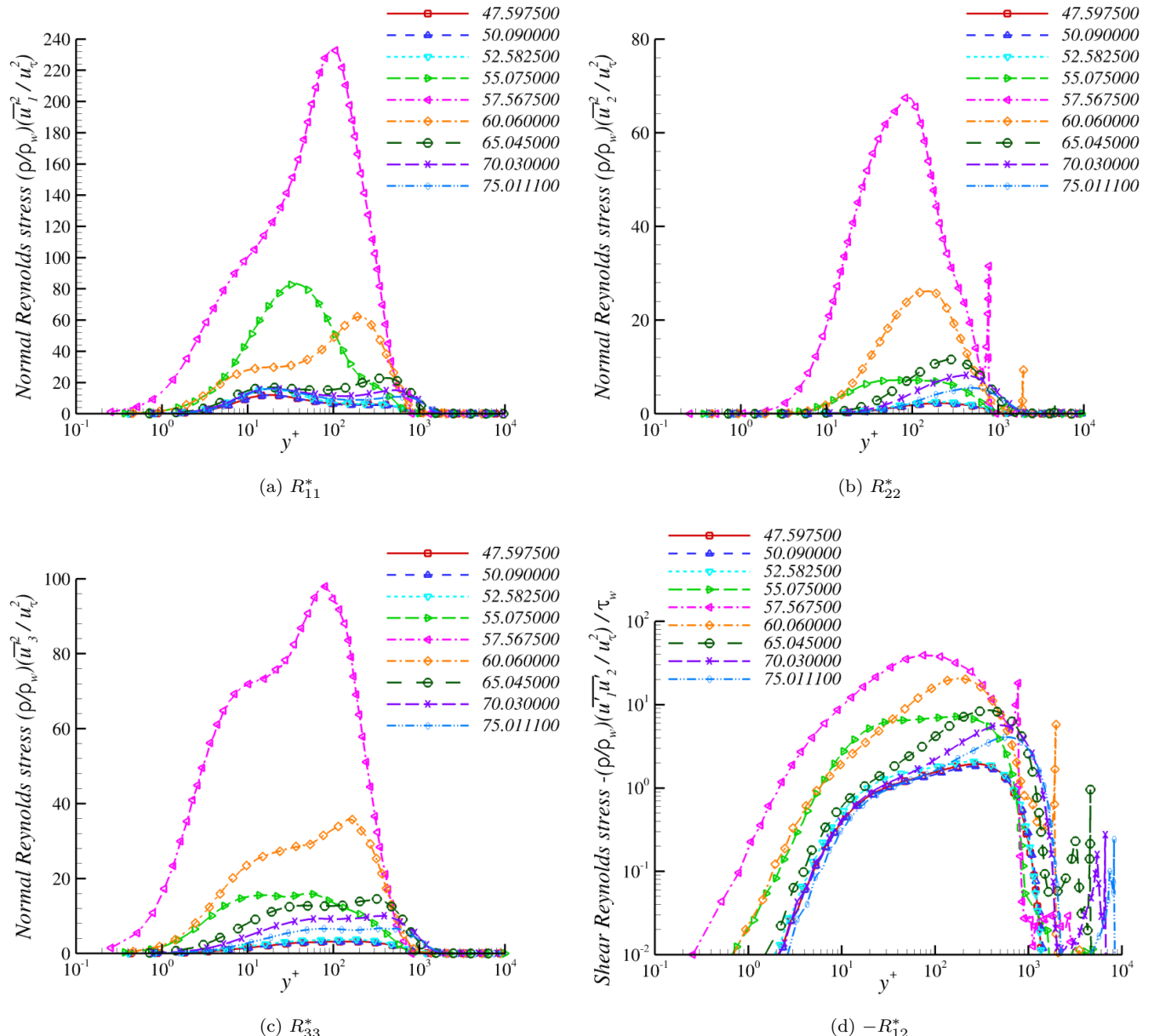


Figure 23: Normalized Reynolds stresses at various streamwise locations

Table 6: Surface Pressure Measurement Locations.

Location	Non-Dimen. by $L_{sep,comp.}$	Computational
1	-1.41	51.187
2	-1.19	52.583
3	-0.96	53.978
4	-0.73	55.474
5	-0.49	56.969
6	-0.04	59.761

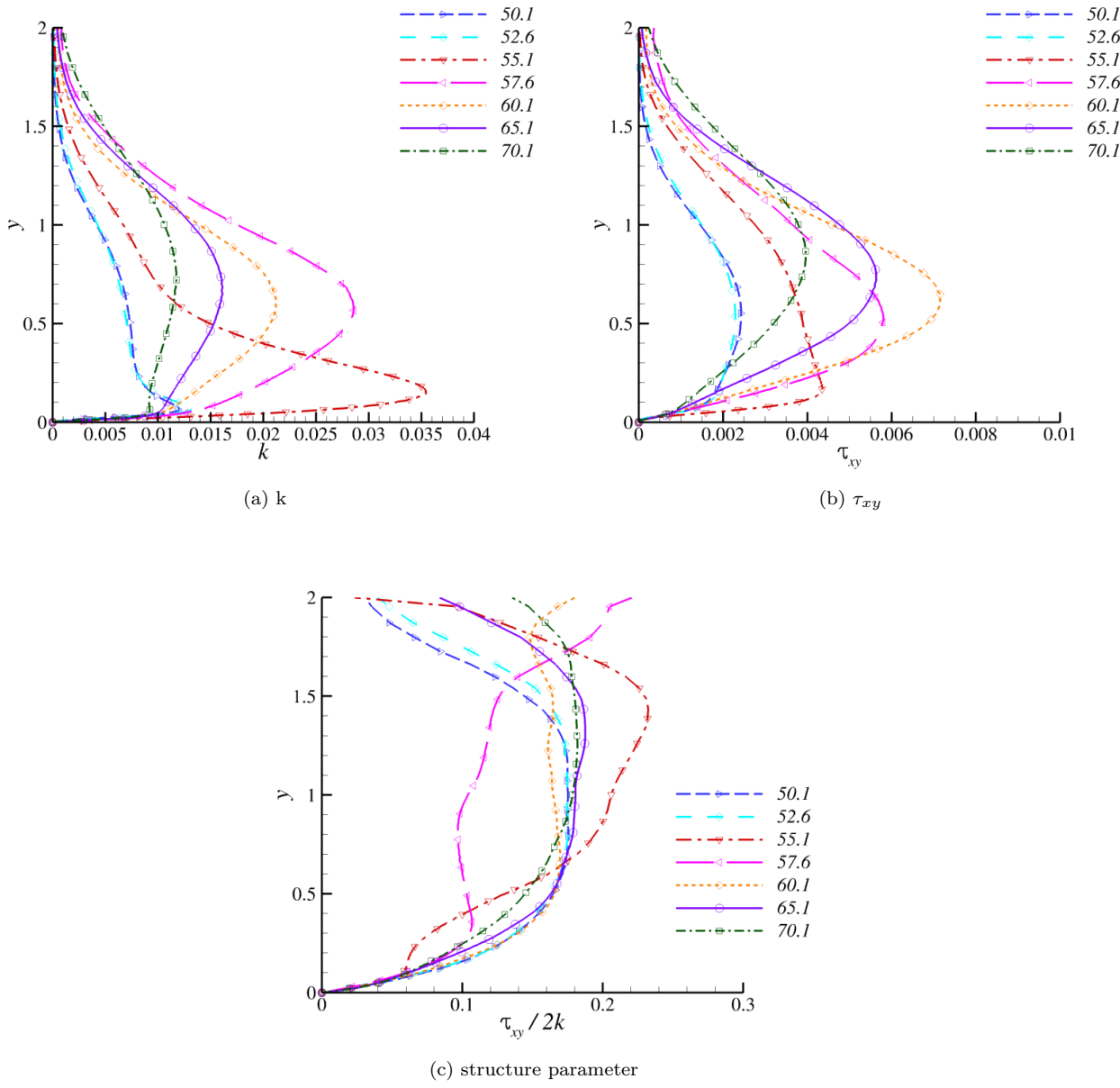


Figure 24: Examination of turbulence amplification

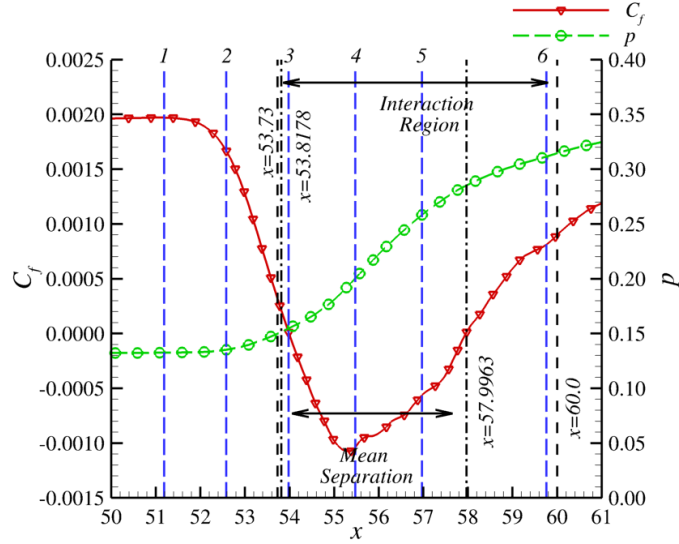


Figure 25: Skin friction and surface pressure within the interaction region

just within the mean separated flow (shown in Fig. 26a) show a visibly discernible low frequency oscillation at a $St_{L_{int,comp}} \sim 0.03$. Figure 26b shows the signal for the remaining three locations. The rms of the fluctuations are (in dimensional units) 73.5, 75.3, 134.5, 134.5, 283.3, 398.0, and 362.2 Pa in ascending order of streamwise measurement location, which again shows amplification ($\sim 5\times$ the incoming value for p'_{rms} versus $\sim 2\times$ the value for p) of the statistical quantities within the interaction.

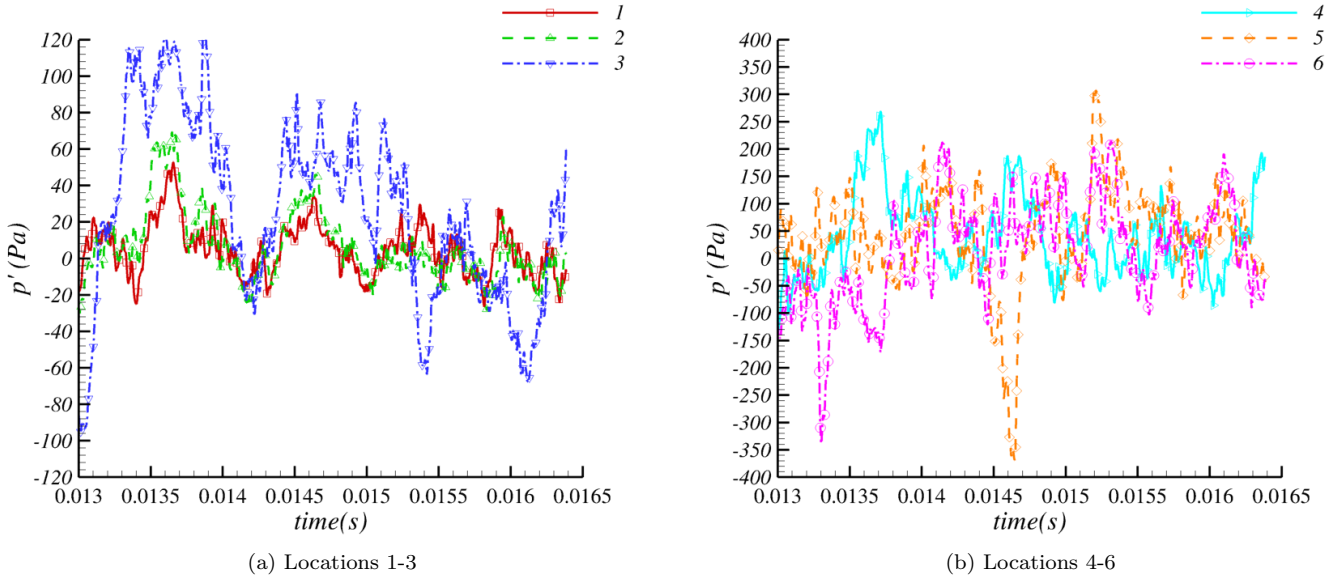


Figure 26: Low-pass filtered pressure fluctuations

To confirm the presence of the low frequency content within the interaction, a Power Spectral Density (PSD) (Fig. 27) was computed for the dimensional pressure fluctuations at each measurement location, as well as the separation location along the centerline. This PSD was conducted by first passing the signal through a lowpass filter with a cutoff frequency of $St \sim 0.25$ and using two rectangular windows with 50%

overlaps. Each measurement shows a peak in the signal at a $St_{L_{int,comp}} \sim 0.036$, which is consistent with the lowest frequency component identified by Ref. 4.

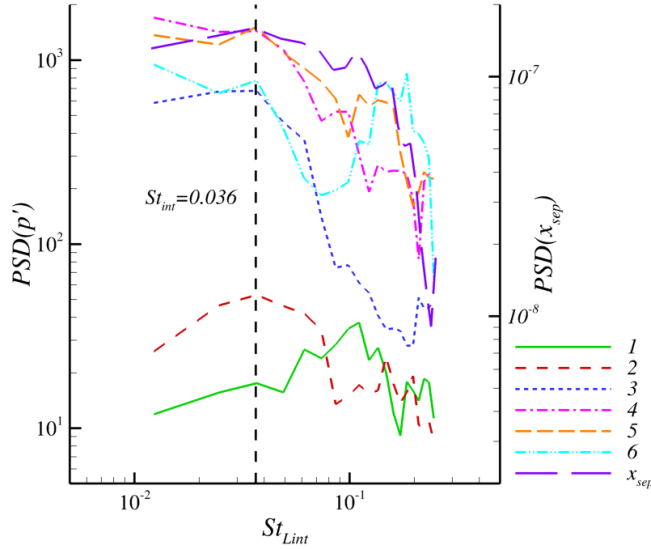


Figure 27: **PSD of pressure and separation point**

The frequency content of the pressure signals can be compared to the experimental results by using a normalized and weighted PSD (as shown in Fig. 28). The computational results were low pass filtered ($St_c = 0.2$ for locations 1-3 and $St_c = 1.0$ for 4-6) and then processed using Welch's method with a Hamming window and 85% overlaps for the first three point probes to get enough realizations of the low frequency content and 50% overlaps for the last three. These signals were then weighted and normalized using:¹⁷

$$\begin{aligned} PSD_{wt}(f) &= f * PSD(f) \\ PSD_{n,wt}(f) &= \frac{PSD_{wt}(f)}{\int_0^\infty PSD_{wt}(\varphi)d\varphi}, \end{aligned} \quad (10)$$

and the computational peaks were scaled to achieve the same peak value as the experimental results. The experimental data is represented with symbols spaced at 3% intervals, and the LES data is shown using lines. All of the computational results show the broadband character expected from the experiment. The computational results at the first three locations have a resolution of $St_{Lint} \sim 0.025$, and the computational peak of location 2 and 3 ($St_{Lint} = 0.047$) are within this resolution of the experimental peaks at $St_{Lint,2} \sim 0.035$ and $St_{Lint,3} \sim 0.064$. At the three locations further downstream, the the results are even more closely matched. This shows that the computations are capturing the unsteadiness of the pressure fluctuations, with the peak moving towards the expected “higher” frequency component of $St_{Lint} \sim 0.5$ as the measurement location proceeds through the interaction region. This further illustrates that the properties of the interaction scale with the interaction length scale.

Figure 29 shows the instantaneous separation and reattachment points for the centerline. These values were determined by the first point where $C_f \leq 0$ (separation), and the last point where $C_f \geq 0$ (reattachment). The rms of the separation point fluctuation is 0.6792 (in non-dimensional units), which is 44% of the boundary layer thickness just before the beginning of the interaction region (or 2.6 times the incoming displacement thickness), which compares with the DNS of a separated turbulent boundary layer of Na and Moin.³⁴

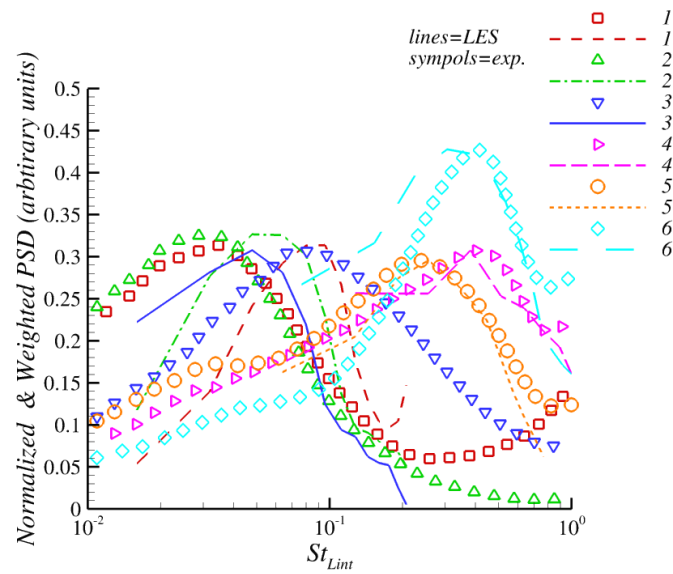


Figure 28: Normalized and weighted PSD comparison between LES and experiment.

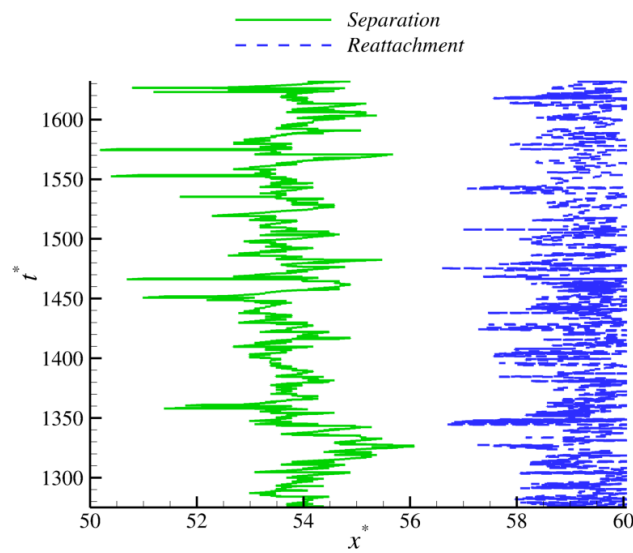


Figure 29: Instantaneous separation and reattachment points along centerline.

Spanwise autocorrelations of the velocity and density fluctuations taken at $y/\delta_{99.0} = 0.25$ are shown in Fig. 30. Several streamwise locations are reported spanning the range from the start of the interaction, through separation, reattachment and the inviscid shock impingement location. Figure 30a shows that the u-velocity fluctuations are decorrelated by $r_z = 1.0$ throughout the interaction, and indicates that within the interaction, the integral length scale (the integral of the plotted function) first narrows ($x = 55$), and then widens ($x = 57.5$). The trends are similar for all variables. Note however that the density fluctuations (Fig. 30d) show the biggest growth in spanwise scales showing the possibility that even though the domain is wide enough upstream of an interaction, the width may need to be increased in order to allow for adequate decorrelation downstream. The growth in scales is also confirmed in Sec. IV.B.3 where coherent structures are discussed.

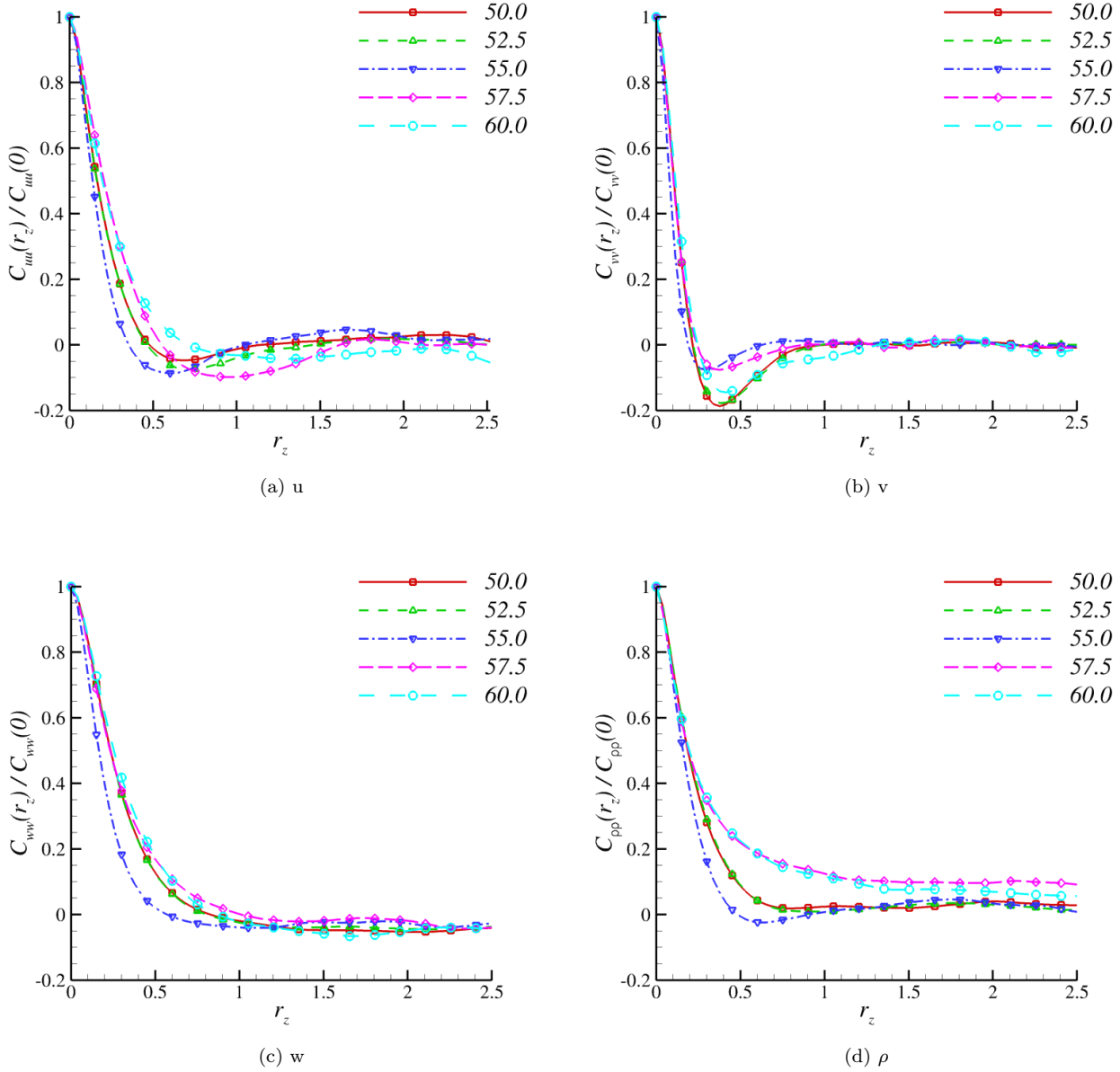


Figure 30: Spanwise autocorrelations in interaction region

Examination of two point correlations in the streamwise direction shows the same trend for first contrac-

tion and then expansion of the length scales. Figure 31 demonstrates this for the pressure fluctuations at the same $y/\delta_{99,0} = 0.25$. The change in scale is on the order of $0.5\delta_{99,0}$. Note that the grid support is maintained at greater than 20 points even at its narrowest.

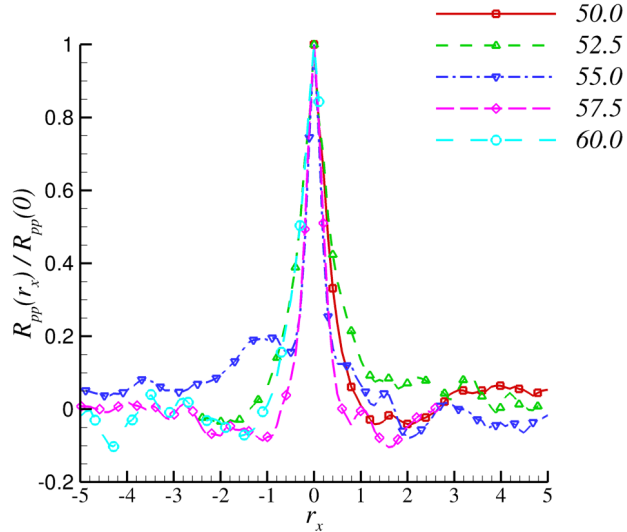


Figure 31: **Two-point correlation of pressure fluctuations**

IV.B.3. Coherent Structures

Instantaneous isosurfaces of the Q-criterion ($Q = 0.5$), colored by the distance from the wall are shown in Fig. 32, with a background of $|\nabla \rho|$, and a isosurface of $|\nabla p|$ (purple) highlighting the shock location. Hairpin vortices can be seen in the incoming boundary layer. These pass through the shock, and become magnified both in amplitude and spanwise extent downstream of the interaction.

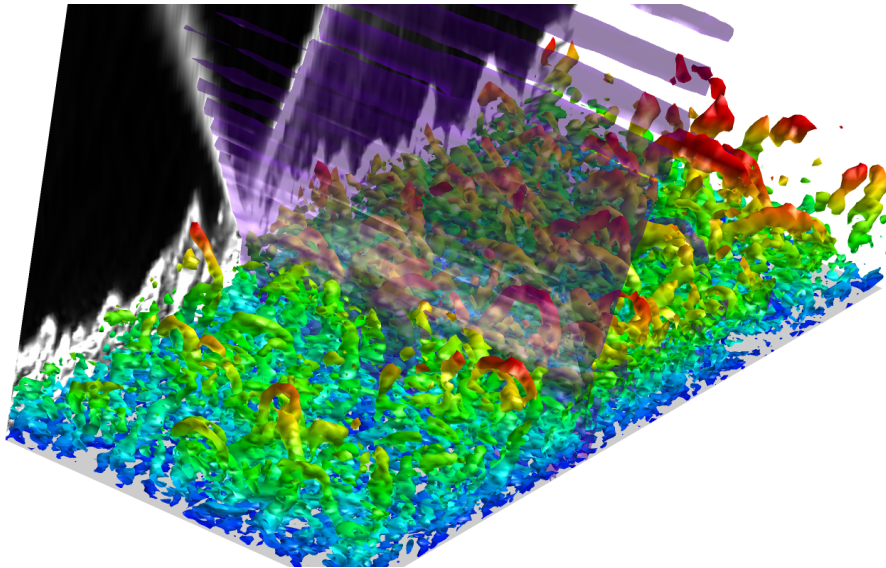


Figure 32: **Coherent Structures near the interaction region**

Figure 33 shows the same data with three hairpin structures isolated. The first is just upstream of the interaction and is used as a baseline. The second structure is within the interaction region and shows the narrowing that was indicated in the correlation data reported in the previous section. The third and final hairpin shows that the structure has significantly widened again showing agreement with the correlation data.

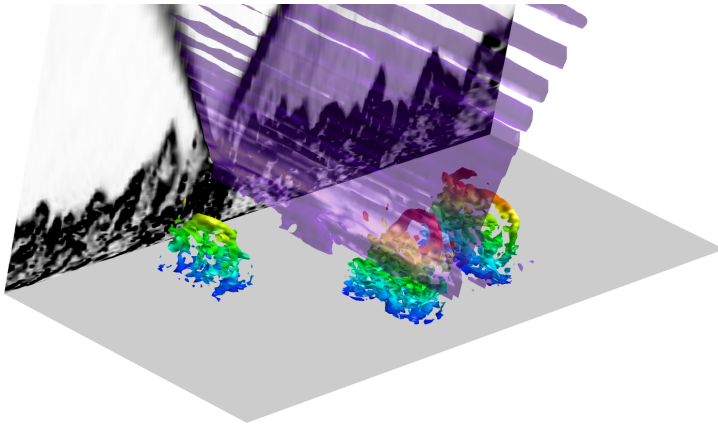


Figure 33: Isolated structures in the interaction.

IV.C. STBLI with control

Results from a preliminary study of the effects of the LAFPAs (simulated as thermal bumps) on the STBLI are presented below. The location and sizing of the thermal bumps (light gray rectangles) is shown in Fig. 34, along with instantaneous contours of u -velocity to show the interaction region. Table 7 shows the properties of the simulated LAFPAs; note that the actuator pulsing frequency is chosen to be equal to the peak frequency identified in the downstream portions of the interaction (pressure tap 6 in Fig. 28).

Table 7: Selected properties of the simulated LAFPAs.

Property	Value
x_{center}	52.6
length	0.75
width	0.5
spacing	1.0
$T_{actuator}$	3.5
$St_{actuator}$	0.5
Duty Cycle	50%

A comparison of the spanwise averaged mean skin friction from the baseline and control cases is provided in Fig. 35. The controlled case separates at $x = 54.37$, vs. $x = 53.82$ for the baseline. Interestingly the mean reattachment occurs at the same location for each case. The change in the separation location yields a reduction in the average separation length of $\sim 10\%$. A localized increase in skin friction occurs in the region of the actuator. The control case skin friction shows a bifurcation in the center of the separation, whereas the baseline does not.

Profiles of the mean temperature and Van Driest transformed velocity are shown in Fig. 36. Figure 36a shows the velocity profiles prior to separation, which show that the baseline case is deviating from the law

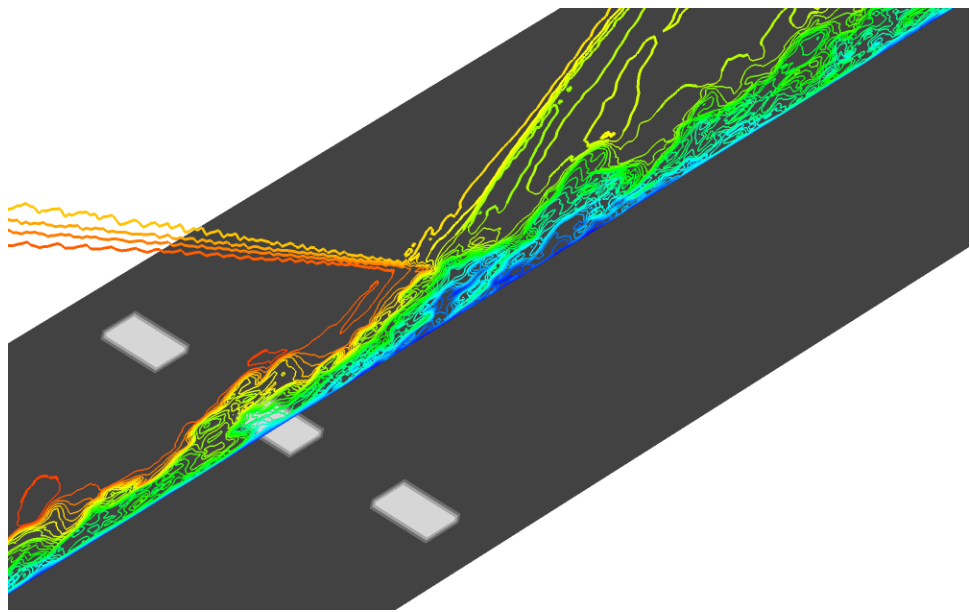


Figure 34: Instantaneous view of STBLI showing simulated LAFPA locations and sizing.

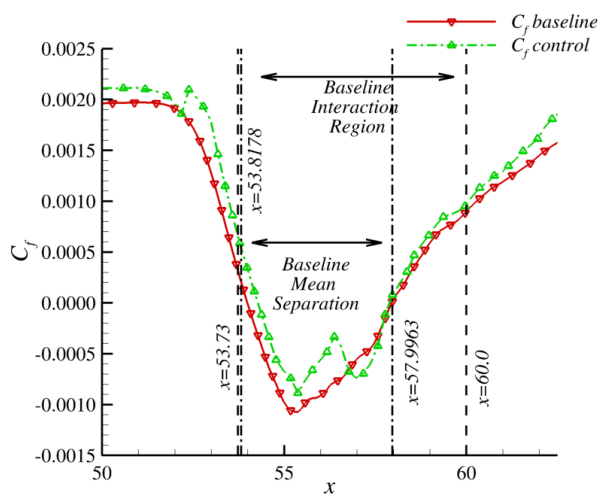


Figure 35: Comparison of mean separation

of the wall at the control location ($x = 52.6$), while the controlled case has not yet shifted. At $x = 53.6$, the control case is shown to be delayed in evolution compared to the baseline case. The differences begin to minimize as the flow moves through the separated region and reattaches (Fig. 36b).

Temperature data prior to separation (Fig. 36c) shows change due to the actuator (at $x = 52.6$), which heats the laminar sub-layer. This temperature difference decreases in magnitude, but remains until the flow separates. This points to the control mechanism for these parameters being a temperature increase near the wall which causes an increase in the local viscosity (which leads to the spike in the skin friction shown previously in the neighborhood of the actuator). In the separated region (Fig. 36d), the temperature profiles of the control and baseline cases follow the same qualitative behavior.

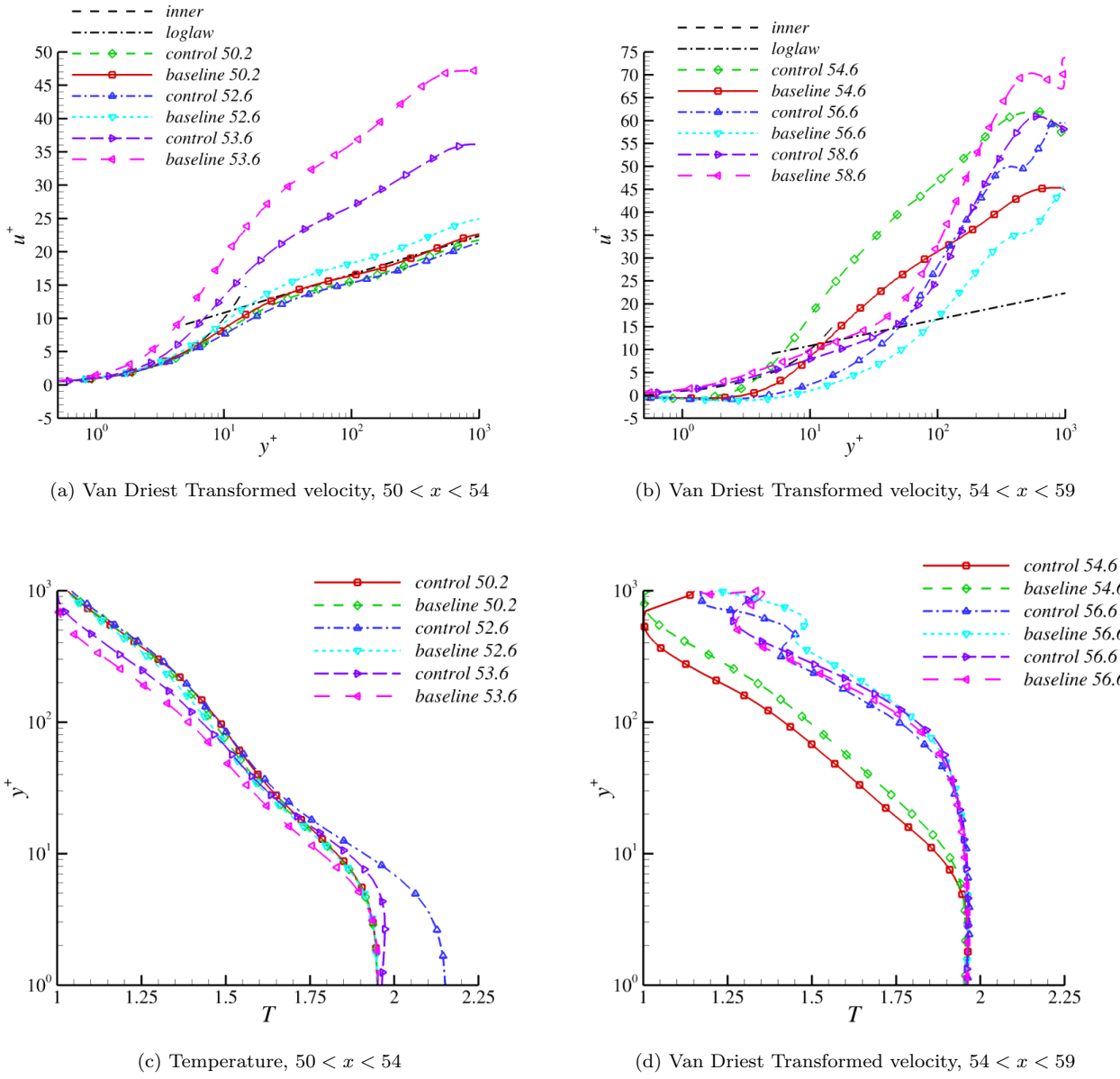


Figure 36: Profiles of flow variables at various streamwise locations

Figure 37 presents a comparison of the surface oil flows between the baseline case (Fig. 37a), and the control case with the actuators on (Fig. 37b) and off (Fig. 37c). The wall is colored by the surface temperature, and the background shows contours of $|\nabla \rho|$ to highlight the shocks and boundary layer structures.

The mean separation and reattachment points are labeled, and regions of negative velocity at the first point above the surface are shaded. The reduction in the length of the separation region is evident between the baseline and control cases. However there do not seem to be significant differences between the separation when the actuator is on and when it is off for the control case.

The three dimensional character of the instantaneous separation is shown in Fig. 38, using an isosurface of $u = 0$ colored by distance from the wall. The baseline case (Fig. 38a) shows distinct peaks of separated flow divided by troughs of attached or negligibly separated flow. The control cases (on in Fig. 38b and off in 38c) again show the separation length decreased, but no significant difference in the three dimensionality of the separation.

Taken together Figs. 35-38 provide a preliminary indication that the current actuator parameters are providing control of the separation length (in fact causing a significant decrease) via a heating effect and not due to the pulsing frequency. An ongoing simulation is being conducted to obtain a long enough simulation time to perform frequency analysis. This frequency analysis will be used to determine what if any effect the actuators are having on the unsteadiness.

V. Conclusions

Large Eddy Simulations are employed to understand shock/turbulent boundary layer interactions. A recently developed approach to generate a spatially developing turbulent boundary layer is further advanced to overcome prior limitations on thermal boundary conditions. A technique based on the generalized stability parameter is presented to efficiently determine adequacy of the size of the force-based trip on a small domain. The method is successfully tested for different Mach and Reynolds number parameters. The method is then employed to examine the STBLI obtained with an impinging oblique shock due to a 9 degree wedge. The setup reproduces experiments performed at The Ohio State University Gas Dynamics and Turbulence Lab. Mean properties of the simulated interaction correspond to those of the interaction when scaled by the incoming boundary layer height. The results confirm prior simulations with other techniques that reproduce the low frequency oscillations of the interaction. Successful comparisons with experimental data are then leveraged to advance the state of understanding of the dynamics. Details of the turbulence amplification and changes in its structure due to extra strain rates encountered in the interaction are discussed, with emphasis on relaxation processes. Coherent structures are shown that have their size and orientation modified by the interaction, with a decrease in length scales followed by an increase as the flow proceeds through the interaction. An array of pulsed thermal bumps (used to model the behavior of LAFPA actuators) is shown to decrease the length of the separation by 10% when pulsed at a frequency close to the peak frequency of the pressure tap measurements in the downstream half of the interaction. Examination of the flow indicate that this reduction is most likely due to a heating effect confirming prior experimental conclusions. Ongoing simulations are being conducted to gather sufficient data to conduct frequency analysis on the controlled interaction in order to determine what if any effect on the unsteadiness is provided by the control method. Future work will include a parametric study of actuator pulsing frequency and temperature to identify possible control strategies.

Acknowledgments

This work has been supported by AFOSR (Monitor: Dr. John Schmisser) and the Ohio Research Scholars Program. The authors acknowledge grants of HPC time from the DOD Supercomputing Resource Centers (DSRCs) at AFRL and ERDC ,and from the Ohio Supercomputer Center. The authors are grateful for many fruitful discussions with N. Webb, M. Samimy and M. Visbal.

References

¹Dolling, D., "Fifty Years of Shock-Wave/Boundary-Layer Interaction Research: What Next?" *AIAA Journal*, Vol. 39, 2001, pp. 1517-1531.

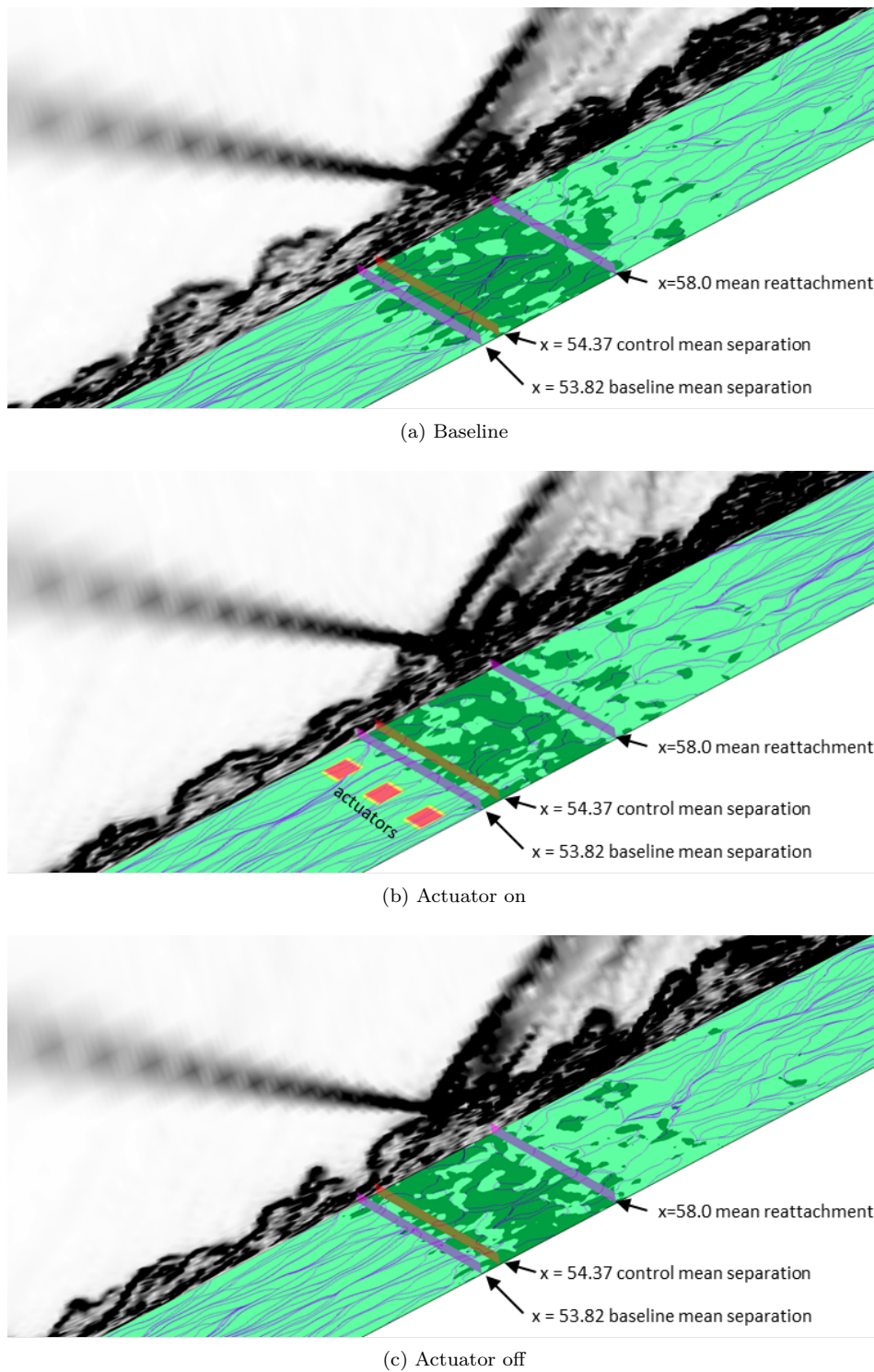


Figure 37: Comparison of Instantaneous Surface Oil Flows and Separation

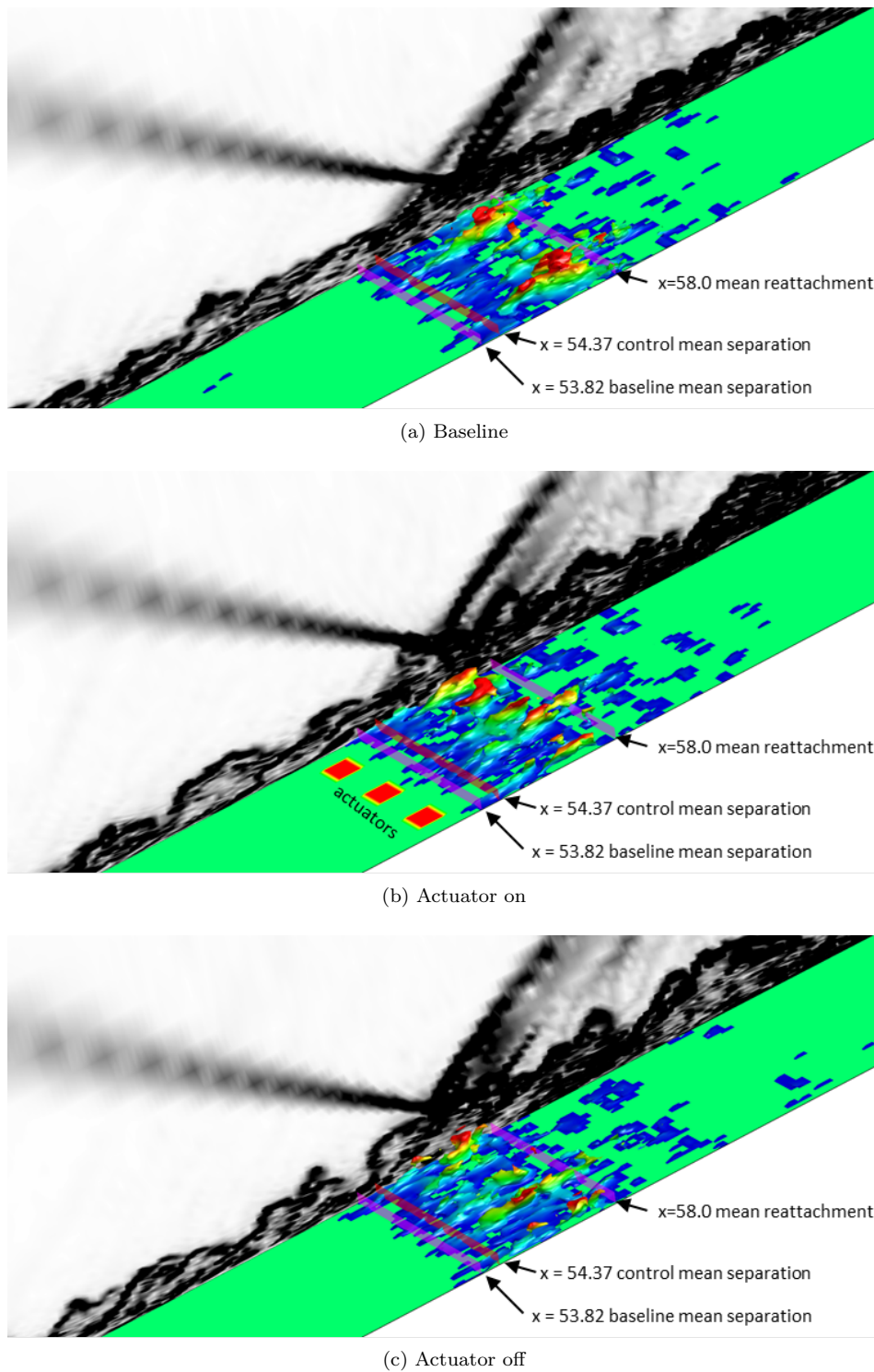


Figure 38: Comparison of Three Dimensional Separated Regions

- ²Delery, J. and Dussage, J.-P., "Some physical aspects of shock wave/boundary layer interactions." *Shock Waves*, Vol. 19, 2009, pp. 453–468.
- ³Dussage, J.-P., Dupont, P., and Debieve, J., "Unsteadiness in shock wave boundary layer interactions with separation," *Aerospace Science and Technology*, Vol. 10, No. 2, 2006, pp. 85–91.
- ⁴Dupont, P., Haddad, C., and Debieve, J. F., "Space and time organization in a shock-induced separated boundary layer," *Journal of Fluid Mechanics*, Vol. 559, 2006, pp. 255–277.
- ⁵Dupont, P., Piponniau, S., Sidorenko, A., and Debieve, J., "Investigation by Particle Image Velocimetry Measurements of Oblique Shock Reflection with Separation," *AIAA Journal*, Vol. 46, 2008, pp. 1365–1370.
- ⁶Ganapathisubramani, B., Clemens, N. T., and Dolling, D. S., "Low-frequency dynamics of shock-induced separation in a compression ramp interaction." *Journal of Fluid Mechanics*, Vol. 636, 2009, pp. 397–425.
- ⁷Edwards, J., "Numerical simulations of shock/boundary layer interactions using time-dependent modeling techniques: A survey of recent results." *Progress in Aerospace Sciences*, Vol. 44, 2008, pp. 447–465.
- ⁸DeBonis, J., Oberkampf, W., Wolf, R., Orkwis, P., Turner, M., and Babinsky, H., "Assessment of CFD Models for Shock Boundary-Layer Interaction," *AIAA 2010-4823, 28th AIAA Applied Aerodynamics Conference*, Chicago, IL, June 28 - July 1 2010.
- ⁹Martin, M. P., Priebe, S., and Wu, M., "Upstream and downstream influence on the unsteadiness of STBLI using DNS data in two configurations," *AIAA-2008-719, 46th AIAA Aerospace Sciences Meeting and Exhibit*, Reno, NV, Jan. 7-10 2008.
- ¹⁰Pirozzoli, S. and Grasso, F., "Direct numerical simulation of impinging shock wave/turbulent boundary layer interaction at $M=2.25$," *Physics of Fluids*, Vol. 18, No. 6, 2006, pp. 065113-1 – 065113-17.
- ¹¹Touber, E. and Sandham, N. D., "Oblique Shock Impinging on a Turbulent Boundary Layer: Low-Frequency Mechanisms," *AIAA-2008-4170, 38th Fluid Dynamics Conference and Exhibit*, Seattle, Wa, June 23-26 2008.
- ¹²Touber, E. and Sandham, N., "Comparisons of three large-eddy simulations of shock-induced turbulent separation bubbles." *Shock Waves*, Vol. 19, 2009, pp. 469–478.
- ¹³Priebe, S., Wu, M., and Martín, M., "Direct Numerical Simulation of a Reflected-Shock-Wave/Turbulent-Boundary-Layer Interaction," *AIAA Journal*, Vol. 47, 2009, pp. 1173–1185.
- ¹⁴Agostini, L., Larchevêque, L., Dupont, P., Debièvre, J.-F., and Dussage, J.-P., "Zones of Influence and Shock Motion in a Shock Boundary Layer Interaction," *AIAA-2011-728, 49th AIAA Aerospace Sciences Meeting including the New Horizons Forum and Aerospace Exposition*, Orlando, FL, Jan. 4-7 2011.
- ¹⁵Beekman, I. B., Priebe, S., Kan, Y.-C., and Martin, M. P., "DNS of a Large Domain, Mach 3 Turbulent Boundary Layer: Turbulence Structure," *AIAA-2011-753, 49th AIAA Aerospace Sciences Meeting including the New Horizons Forum and Aerospace Exposition*, Orlando, FL, Jan. 4-7 2011.
- ¹⁶Caraballo, E., Webb, N., Little, J., Kim, J.-H., and Samimy, M., "Supersonic Inlet Flow Control Using Plasma Actuators," *AIAA-2009-924, 47th AIAA Aerospace Sciences Meeting including The New Horizons Forum and Aerospace Exposition*, Orlando, FL, Jan. 5-8 2009.
- ¹⁷Webb, N., Clifford, C., and Samimy, M., "Preliminary Results on Shock Wave/Boundary Layer Interaction Control Using Localized Arc Filament Plasma Actuators," *AIAA-2011-3426, 41st AIAA Fluid Dynamics Conference and Exhibit*, Honolulu, HI, June 27-30 2011.
- ¹⁸Yan, H. and Gaitonde, D., "Effect of thermally induced perturbation in supersonic boundary layers," *Physics of Fluids*, Vol. 22, No. 6, 2010, pp. 064101.
- ¹⁹Gaitonde, D. and Samimy, M., "Coherent structures in plasma-actuator controlled supersonic jets: Axisymmetric and mixed azimuthal modes," *Physics of Fluids*, Vol. 23, 2011, pp. 095104.
- ²⁰Pirozzoli, F., Grasso, F., and Gatski, T. B., "Direct numerical simulation and analysis of a spatially evolving supersonic turbulent boundary layer at $M=2.25$," *Physics of Fluids*, Vol. 16, No. 3, 2004, pp. 530–545.
- ²¹Mullenix, N. J., Gaitonde, D. V., and Visbal, M. R., "A Plasma-Actuator-Based Method to Generate a Supersonic Turbulent Boundary Layer Inflow Condition for Numerical Simulations," *AIAA-2011-3556, 20th AIAA Computational Fluid Dynamics Conference*, Honolulu, HI, June 27-June 30 2011.
- ²²Mullenix, N. J., Gaitonde, D. V., and Visbal, M. R., "Generation of Turbulent Boundary Layers for the Large Eddy Simulation of Shock Boundary Layer Interactions," *AIAA-2012-, 50th AIAA Aerospace Sciences Meeting including the New Horizons Forum and Aerospace Exposition*, Nashville, TN, Jan. 2012.
- ²³Mullenix, N., Gaitonde, D., and Visbal, M., "Generation of a Spatially Developing Supersonic Turbulent Boundary Layer With a Body Force Based Method," *AIAA Journal*, Vol. accepted, 2013.
- ²⁴Gaitonde, D., Visbal, M., and Roy, S., "Control of Flow Past a Wing Section with Plasma-based Body Forces," *AIAA-2005-5302, 36th AIAA Plasmadynamics and Lasers Conference*, Toronto, Ontario, June 6-9 2005.
- ²⁵Gaitonde, D. and Visbal, M., "High-Order Schemes for Navier-Stokes Equations: Algorithm and Implementation into FDL3DI," Tech. Rep. AFRL-VA-WP-TR-1998-3060, Air Force Research Laboratory, Wright-Patterson AFB, 1998.
- ²⁶Mullenix, N. J. and Gaitonde, D. V., "A Bandwidth and Order Optimized WENO Interpolation Scheme for Compressible Turbulent Flows," *AIAA-2011-366, 49th AIAA Aerospace Sciences Meeting including the New Horizons Forum and Aerospace Exposition*, Orlando, FL, Jan. 4-7 2011.
- ²⁷Visbal, M. R., Rizzetta, D. P., and Matthew, J., "Large-Eddy Simulation of Flow Past a 3-D Bump," *AIAA-2007-917, 45th AIAA Aerospace Sciences Meeting and Exhibit*, Reno, NV, Jan. 8-11 2007.
- ²⁸Smits, A. J. and Dussage, J.-P., *Turbulent Shear Layers in Supersonic Flow*, Springer Science+Business Media, New York, NY, 2nd ed., 2006.
- ²⁹Cebeci, T., *Analysis of Turbulent Flows*, Elsevier, Amsterdam, 2nd ed., 2004.
- ³⁰Perry, A. E. and Li, J. D., "Experimental support for the attached-eddy hypothesis in zero-pressure-gradient turbulent boundary layers," *Journal of Fluid Mechanics*, Vol. 218, 1990.
- ³¹Reed, H., Saric, W., and Arnal, D., "Linear Stability Theory Applied to Boundary Layers," *Annual Review of Fluid Mechanics*, Vol. 28, 1996, pp. 389–428.

³²Yentsch, R. and Gaitonde, D., "Numerical Investigation of Hypersonic Phenomena Encountered in HIFiRE Flight 1," *AIAA 2012-0943, 50th AIAA Aerospace Sciences Meeting including the New Horizons Forum and Aerospace Exposition*, Nashville, TN, Jan. 9-12 2012.

³³Touber, E. and Sandham, N., "Large-eddy simulation of low-frequency unsteadiness in a turbulent shock-induced separation bubble," *Theoretical and Computational Fluid Dynamics*, Vol. 23, 2009, pp. 79–107.

³⁴Na, Y. and Moin, P., "Direct numerical simulation of a separated turbulent boundary layer," *Journal of Fluid Mechanics*, Vol. 374, 1998, pp. 379–405.